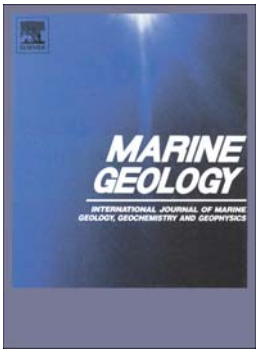

Earthquake-triggered deposits in the subduction trench of the North Ecuador/South Colombia margin and their implication for paleoseismology

S. Migeon, C. Garibaldi, G. Ratzov, S. Schmidt, J.-Y. Collot, S. Zaragosi, L. Texier

PII: S0025-3227(16)30200-6
DOI: doi: 10.1016/j.margeo.2016.09.008
Reference: MARGO 5510

To appear in: *Marine Geology*

Received date: 15 September 2015
Revised date: 2 September 2016
Accepted date: 16 September 2016

Please cite this article as: Migeon, S., Garibaldi, C., Ratzov, G., Schmidt, S., Collot, J.-Y., Zaragosi, S., Texier, L., Earthquake-triggered deposits in the subduction trench of the North Ecuador/South Colombia margin and their implication for paleoseismology, *Marine Geology* (2016), doi: 10.1016/j.margeo.2016.09.008

Earthquake-triggered deposits in the subduction trench of the north Ecuador/south Colombia margin and their implication for paleoseismology

S. Migeon[1-3], C. Garibaldi[1], G. Ratzov[1], S. Schmidt[2], J.-Y. Collot[1], S. Zaragosi[2], L. Texier[3]

(1) Université Nice Sophia Antipolis, CNRS, IRD, Observatoire de la Côte d'Azur, Géoazur UMR 7329, 250 rue Albert Einstein, Sophia Antipolis 06560 Valbonne, France

(2) UMR5805 EPOC, Univ. Bordeaux, Avenue Geoffroy Saint-Hilaire, CS 50023, 33615 Pessac Cedex, France

(3) Sorbonne Universités, UPMC Univ Paris 06, 4 place Jussieu, 75252 PARIS cedex 05, France

Corresponding author: Migeon Sébastien (migeon@geoazur.unice.fr)

Abstract

The north Ecuador/south Colombia convergent margin is affected by recurrent subduction earthquakes with magnitudes greater than 7.5, like the 1906, 1942, 1958, 1979 and 2016 events. The subduction trench is characterized by the construction of the Esmeraldas Turbidite System (ETS) fed by the large Esmeraldas Canyon that deeply incises the continental slope and that connects directly onshore with the Esmeraldas River. The detailed description of cores collected in the left-hand (western) proximal levee of the ETS and in two lobes allowed discriminating two types of coarse-grained deposits: (1) "classical" flood-generated turbidites are normally graded beds with structureless, laminated and cross-laminated intervals and high organic-matter content, while (2) earthquake-induced deposits consist of amalgamated normally-graded laminated/cross-laminated intervals separated by erosive surfaces. These latter are interpreted to be deposited by quasi-synchronous flows generated during a single earthquake. Organic matter is absent in such beds while ferromagnesian minerals and pumices are abundant, suggesting remobilization of the slope deposits. When two amalgamated beds are superimposed, the interbedded clayey interval is not bioturbated, suggesting a short time period between the beds deposition, and thus the impact of a major earthquake shock and following earthquakes on the triggering of landslides.

Along the ETS, core-to-core correlation based on ^{210}Pb excess revealed that 20th Century sedimentation occurred mainly in the proximal levee. There, a temporal relationship was established between the 1906, 1942, and 1979 earthquakes, and three coarse-grained beds showing features of earthquake-induced turbidites, suggesting the Esmeraldas Canyon was the main source for sediments to be remobilized during these earthquakes. The fining and thinning observed between the 1906, 1942 and 1979 turbidites correlate with the increasing distance of the rupture zone of each earthquake with the Esmeraldas Canyon. Earthquakes with magnitudes lower than 7 also affected the margin during the 20th Century but were not recorded in the trench sedimentation, suggesting that the turbidite levee acts as a natural filter so that potentially the highest the levee the strongest the earthquake magnitude recorded. At least ten earthquakes with the highest magnitudes were recorded on the turbidite levee within the last 800 years with a recurrence time ranging from about 280 yrs to 40-70 yrs, or less for the 20th Century earthquakes. The comparison of the main features of the 1906 turbidite with older earthquake-triggered turbidites identified in a core collected in the trench suggests that one or two earthquakes similar to the 1906 event might have occurred ~600 yrs ago.

Keywords: Colombia trench, earthquakes, turbidites, levee, ^{210}Pb excess

1. Introduction

Seismic-hazard assessment is a crucial issue in tectonically active, densely populated regions. Along subduction margins, destructive tsunamis often accompany the damaging effects of great subduction earthquakes (Subarya et al., 2006). In a given area, the recurrence and magnitude of earthquakes are estimated in two ways: (1) the extrapolation of specific events based on the monitoring of the present-day seismicity through permanent or temporary networks, and (2) the analysis of historical-earthquakes together with archeological investigations in the field. In most cases, a mean-earthquake recurrence can be constrained by these techniques over the last 300-500 years. The access to the earthquake recurrence over a longer time period requires the detailed analysis and interpretation of paleoseismic indicators recorded in the sedimentary archives deposited on the sea bed along active margins (Gorsline et al., 2000; Shiki et al., 2000; Noda et al., 2008), on land nearby the coastline, or in lakes (Sims, 1973, 1975; Schnellmann et al., 2002; Monecke et al., 2004; Becker et al., 2005; Fanetti et al., 2008; Avsar et al., 2014; Kempf et al., 2015).

Four main sedimentological evidences are classically used to discriminate earthquake-induced sediment layers from the typical sedimentation of margins or lacustrine infillings. There are (1) soft-sediment deformation structures related to liquefaction processes due to the remobilisation of pore water during episodes of ground acceleration (Rossetti, 1999; Vanneste et al., 1999; Rodriguez-Pasqua et al., 2000; Smoot et al., 2000), (2) homogenised sediment layers (called homogenites) resulting from an oscillatory movement of the whole water column, known as a seiche effect, in semi-enclosed or enclosed basins (Chapron et al., 1999; Beck et al., 2007), (3) coarse-grained deposits resulting from the triggering of landslides and their potential transformation into turbulent flows such as turbidity currents (Nakajima and Kanai, 2000; Goldfinger et al., 2003; Moernaut et al., 2007; Masson et al., 2011; Ratzov et al., 2015), and (4) coastal and lagoon deposits emplaced by tsunami triggered during earthquake events (Nelson et al., 2006; Kempf et al., 2015).

Soft-sediment deformation structures and homogenites are relatively easy to identify from outcrops or cores but can be difficult to date accurately due to the in-situ reworking of pre-existing deposits. Such features were successfully used in lakes to investigate the record of historical earthquakes and to reconstruct earthquake recurrences (Sims, 1975; Monecke et al., 2004; Avsar et al., 2014). Tsunami, when they are caused by earthquakes, can be associated to both local and distant events as they are able to cross entire oceans, so it is still problematic to use tsunami deposits to build a local earthquake model (Nelson et al., 2006). The

sedimentological characteristics of submarine mass-transport deposits (MTD) and turbidites are now well constrained from the study of sediment cores collected at sea (Mulder and Alexander, 2001; Tripsanas et al., 2008) and in lakes (Girardclos et al., 2007; Waldmann et al., 2011), and these deposits can be accurately dated when they are interbedded with hemipelagic foram-rich or wood-fragments-rich layers, or tephras. Although earthquakes are known to be a specific triggering factor of submarine landslides and gravity flows, other factors like eustatism, floods, and storms are also invoked (Mulder et al., 2001a; Mulder et al., 2001b; St-Onge et al., 2004; Maslin et al., 2005; Piper and Normark, 2009). Although a few criteria were already established to attempt discriminating earthquake-induced turbidites from "classical" turbidites (i.e. turbidites triggered by sediment overloading/gravity or flood activity), like the presence of amalgamated beds (Nakajima and Kanai, 2000; Noda et al., 2008), the relationship between turbidites and earthquakes in both marine and lacustrine deposits is mainly based on the precise dating of clastic beds and their correlation with documented earthquakes (Goldfinger et al., 2003; Huh et al., 2004; Huh et al., 2006; Gràcia et al., 2010; Waldmann et al., 2011). Alternately, the most used turbidite paleoseismology approach (Goldfinger et al., 2003; Goldfinger, 2011; Polonia et al., 2013; Pouderoux et al., 2015; Ratzov et al., 2015) is based on the dating of synchronous turbidites over wide areas and independent sedimentary systems, thus requiring a regional trigger, interpreted most likely as an earthquake (Goldfinger et al., 2003).

To date, no sedimentary criteria, that are both reliable and systematic, exist to discriminate co-seismic deposits. A robust identification of such deposits would represent a significant improvement in assessing long time-series of great coastal and submarine earthquakes in order to constrain their recurrence intervals and regularity. In the present study, in addition to multibeam bathymetry/backscatter data, we used four cores collected in the Colombia Trench (Pacific margin) along a segment of the Ecuador-Colombia convergent margin that was affected by four large earthquakes with Mw>7.7 during the 20th Century. From detailed sedimentological analyses and dating, we identified turbidites and particular coarse-grained beds that we interpreted to be earthquake-induced, and defined specific features characterizing such deposits.

2. Geodynamic setting and the 20th Century subduction earthquakes

The north Ecuador-south Colombia margin is underthrust eastwards by the young (<20 Ma) and heterogeneous Nazca plate (Lonsdale, 2005), at a convergence rate of 5.6 cm/yr with respect to South America (Nocquet et al., 2014). The convergence has resulted in strong tectonic deformation reflected in the structural and seismo-tectonic patterns of the margin, the history of which is recorded in fore-arc basin and subduction trench sediments. The largest historical earthquake (Mw 8.8) occurred in 1906 (Kanamori and Given, 1981) and had an estimated rupture zone of ~500 km long (Kelleher, 1972). The rupture zone was partially reactivated by large subduction earthquakes, which occurred from south to north, in 1942 (Mw 7.8), 2016 (Mw 7.8), 1958 (Mw 7.7) and 1979 (Mw 8.2) (Beck and Ruff, 1984; Swenson and Beck, 1996) (Fig. 1). A tele-seismic study of the three large thrust earthquakes (Mendoza and Dewey, 1984) indicate that the1942 event was followed by a 2 months sequence of Mb 5.2-6.0 aftershocks, including 10 Mb 5.4-5.9 events within 3 days after the main quake; a 3-months sequence of 11 Mb 5.2-6.2 events followed the 1958 event, and the 1979 event was followed by a 2-week sequence of 30 Mb 4.8-5.7 events. Ground shaking related to these major events and their aftershock sequences may have caused submarine mass movements across the continental slope as suggested by Ratzov et al. (2010).

3. Data and Methods

The dataset presented in this paper was collected in the Colombia Trench during the AMADEUS cruise (Collot et al., 2005). Both bathymetry and backscatter data were recorded using a hull-mounted Simrad EM12 multibeam system. Raw bathymetry data were processed using the Caraibes software (Ifremer) to obtain a DEM with a spatial resolution of 150 m. Chirp (3-5 kHz) profiles were collected using a hull-mounted system during the EM12 survey.

Piston cores KAMA05, KAMA09, KAMA10 and KAMA21 were collected in the Esmeraldas Turbidite System (ETS), in both levee and lobe environments, at water depth ranging from 2950 to 3700 m (Fig. 1). After splitting and visual description, X-ray images were acquired on 1-cm thick sediment slabs using the SCOPIX system (Migeon et al., 1999) to study the internal structure of the deposits. On these images, darker layers are of higher density. Then, grain-size (Coulter® LS200 laser granulometer) and magnetic susceptibility (Bartington® MS2E sensor) were analyzed every 1-2 cm to characterize and to discriminate the different types of gravity-flow deposits. The granulometric curves shown in this study display the

median value. Additional high-resolution sedimentological and petrographic information was finally obtained from thin sections (100 x 45 x 13 mm) made following the protocol used by Zaragosi et al. (2006). Thin-section images were acquired using a fully automated Leica DM6000 B digital microscope with multiple magnifications and help interpreting the potential sources and origins of the beds.

These descriptions were used to select samples in hemipelagic layers for dating. Dating was based on ^{210}Pb excess ($^{210}Pb_{xs}$) which is incorporated rapidly into the sediment from atmospheric fallout and water column scavenging (Schmidt and De Deckker, 2015). ^{210}Pb and ^{226}Ra activities were measured using a low background γ detector on the uppermost section of cores KAMA21, KAMA09 and KAMA05. Calibration of the γ detector was achieved using IAEA standards (RGU-1, RGTh-1). $^{210}Pb_{xs}$ was calculated by subtracting the measured activity supported by its parent isotope, ^{226}Ra, from the total ^{210}Pb activity in the sediment. Errors in $^{210}Pb_{xs}$ were calculated by propagation of errors in the corresponding pair, ^{210}Pb and ^{226}Ra. Different models are classically used to estimate age of deposits: constant flux-constant sedimentation (CF-CS), constant initial concentration (CIC) and constant rate of supply (CSR) (see Kirchner (2011) among others). In this work, we combined different models to better constrain the age model. First we have used the CIC model which assumes a steady initial $^{210}Pb_{xs}$ concentration at the sediment interface. The CIC age (t) of each measured horizon was calculated according to the following equation (Robbins and Eglington, 1975): $t= (1/\lambda) \ln(A_0/A_z)$ where t and A_z are the age of the sediment and the excess ^{210}Pb activity at the depth z, A_o is the activity at the surface and λ is the decay constant of ^{210}Pb. As it was not always possible to sample about 3 g of dry hemipelagic sediments just above and below each deposits, we have then applied the CF-CS model to better constrain the timescale. The fundamental hypothesis of the CF-CS model is that the $^{210}Pb_{xs}$ flux to the sediment and the sedimentation rates are constant: it implies to subtract the thickness of each gravity-flow deposits to produce an event-free $^{210}Pb_{xs}$ profile. This event-free profile allowed to estimate a mean background of sedimentation rate of 0.97 cm/yr. It must be pointed out that this background sedimentation rate over the last century is almost the same as the one obtained in the upper 25 cm of the core KAMA21, indicating a rather constant intensity of the hemipelagic sedimentation. The ranges of ages, according to the CIC and CF-CS models, agree reasonably. Because hemipelagic layers with sufficient well-preserved foraminifers were never found, ^{14}C dating was done on wood fragments found in gravity-flow deposits in cores KAMA21, KAMA10 and KAMA05 (Table 1).

4. Geomorphology of the north Ecuador/south Colombia margin

The north Ecuador/south Colombia margin is eroded by two main canyons, the Esmaraldas Canyon to the south west and the Patia Canyon to the north east, which supply the trench with significant amounts of sediment (Fig. 1). The former built the 250-km long Esmeraldas Turbidite System in the subduction trench (Collot et al., 2005) while the latter fed the 30-km long Patia Fan (Ratzov et al., 2012)(Fig. 1). The head of the Esmeraldas Canyon is connected to the estuary of the Esmeraldas River, allowing direct supply of continental materials to the deep sea during episodes of floods, like the ones generated during El Niño periods. In deeper waters, the canyon is 300 to more than 1000 m deep; it should strongly confine sediment supply and gravity flows that are mainly delivered to the trench, the continental slope being a by-pass area. Several semi-circular or linear scars related to submarine landslides are located along the canyon or affect the continental slope at various water depths (Fig. 1). They are 5 to 15-km long, 20 to 300 m in height, and represent volumes of missing material ranging from $1x10^8$ to $8x10^9$ m^3. A SW-NE trending sub-linear scarp, 110-190 m high, is interpreted as the morphological expression of the deep Ancon Fault (Fig. 1)(Collot et al., 2005; Collot et al., 2008). The northern termination of the fault is characterized by a large divergent network of dominantly seaward-facing subvertical normal faults. They intensively fracture the margin, and may lead to the gradual destabilisation of the continental slope (Ratzov et al., 2007).

The Esmeraldas Canyon cuts through a 10 km-wide accretionary prism (Collot et al., 2008), at about 2700 m of water depth. From there, the particle supply in the subduction trench is deflected either to the west, feeding the small Esmeraldas Fan, or to the north-east and feeding the trench-parallel Esmeraldas Turbidite System (ETS) (Fig. 1). In the ETS, a first segment of the Esmeraldas Channel (EC1 in Fig. 1) extends to the north-northeast over 80 km from the mouth of the canyon to 3350 m of water depth. It is 2 km wide and changes down-flow from a meandering to a more linear planform pattern (Fig. 1).

The EC1 is bounded to the right and the left by sediment accumulations, 15-20 km wide (Fig. 1), characterized by a well-layered and continuous echofacies (Fig. 2). They are interpreted as levees. Their height above the channel floor decreases from 100 m to less than 10 m downchannel. In plan view, the two levees exhibit a wavy pattern that mimics the morphology of the meanders (Fig. 1). The wavy structures are asymmetrical in shape (Fig. 2). Reflectors are parallel and continuous on their upstream flanks and stop abruptly through erosive

truncations on their downstream flanks. Correlation of reflectors across every structure shows that sediment thickness is 2-3 times higher on their upstream than their downstream flanks (Fig. 2). Such features are typical of sediment waves (Normark et al., 2002; Migeon et al., 2004). The presence of sediment waves suggests high sediment supply through time on the levees (Migeon et al., 2000).

In its distal part, the channel gradually smoothens and terminates in a flat trench area. The backscatter imagery reveals an area characterized by patches with high-backscatter (black) and low-backscatter (white) acoustic facies contrasting with the homogeneous medium-backscatter (grey) acoustic facies of the trench (Fig. 1). The patches are mostly elongated in the direction of flows coming out from EC1. Within this area, echofacies consists of a strong reflection at the seafloor with no or little signal penetration of the signal (Fig. 2), suggesting the presence of surficial sandy deposits (Zaragosi et al., 2000). From similarities with published results (Schwab et al., 1996; Unterseh et al., 1998; Kenyon et al., 2002; Migeon et al., 2010), this area is interpreted to be a depositional lobe (Lobe 1 in Fig. 1). Lobe 1 is 40 km long, 20 km wide.

A second segment of the Esmeraldas Channel develops at the north-eastern edge of Lobe 1 (EC2 in Fig. 1), at 3600 m water depth. It is 40 km long, 2 km wide and 10 m deep. It is bounded to the east by the Patia Fan (Fig.1). It terminates at 3720 m water depth in a flat trench area where the backscatter imagery reveals the presence of a depositional lobe (Lobe 2 in Fig. 1) with features similar to those previously described at the mouth of EC1. Lobe 2 is 60 km long and 15 km wide.

5. General description of cores and age model

Four cores were collected along the ETS (Figs 1 and 3). Core KAMA21 (8.2 m long) is located near the crest of the left-hand levee, in the upper part of EC1 (Figs 1 and 3). Cores KAMA10 (1.8 m long) and 09 (7.6 m long) were collected in the proximal part and the distal fringe of Lobe 1, respectively (Figs 1 and 3). Core KAMA05 (4.7 m long) was collected in the distal part of Lobe 2 (Figs 1 and 3).

The four cores consist of silty/sandy beds 2-60 cm thick alternating with muddy intervals (Fig. 3). The sandy beds can be structureless, laminated, cross-laminated, or with floating mud clasts. Their abundance is also variable depending on the location of cores: sandy-bed

content is about 10% in core KAMA09, 35% in core KAMA21, 52% in core KAMA05, and 85% in core KAMA10.

Core KAMA21 shows significant $^{210}Pb_{xs}$ levels down to about 140 cm, suggesting these sediments have been deposited since AD 1900 (Fig. 4). In this core interval, four coarse-grained beds (B1 to B4 in Fig. 4) were identified, in particular a thick one (B1) between 27 and 52 cm (Fig. 4). Excesses of ^{210}Pb just above and below this layer are comparable, confirming an instantaneous deposition. Considering only hemipelagic intervals identified using X-rays images (lighter intervals), the mean hemipelagic sedimentation rate would be about 0.97-1.1 cm/yr (Fig. 4a-b). Based on the combination of both CIC and CF-CS ^{210}Pb-dating (Fig. 4c), we assume B1 to have been deposited in AD 1980 ±4, B2 in AD 1962 ±7, B3 in AD 1948 ±7, and B4 in AD 1912 ±12. Then, the age model was extended downcore using the two ^{14}C dates giving historical ages (Table 1; Fig. 3). Because core KAMA21 was collected on a levee and because coarser beds do not exhibit erosive base, there was no or little erosion of the hemipelagic mud sedimentation. So considering again hemipelagic intervals only, the mean hemipelagic sedimentation rate was estimated at 0.16 ± 0.007 cm/yr between 140 and 342 cm of depth and at 0.35 ± 0.024 cm/yr between 342 and 521 cm of depth. The absence of $^{210}Pb_{xs}$ on top of cores KAMA09 and KAMA05 suggest no or very little recent sedimentation. In KAMA10 and KAMA05, ^{14}C dates still give an historical age (Table 1; Fig. 3). Considering hemipelagic intervals only, a mean sedimentation rate of 0.02 cm/yr and 0.04 cm/yr was estimated in cores KAMA10 and KAMA05, respectively, but because of the abundance of thick sandy beds with erosive bases, the age model in each core is not considered robust enough to correlate beds with core KAMA21.

6. Lithological characteristics of gravity-flow deposits

In addition to the hemipelagic clayey beds, four main types of coarser-grained beds were discriminated from the study of the four cores.

Beds of Type 1 consist of a basal sandy layer grading upward into a dark clayey-silty interval then a light clayey interval (Figs 5 and 6). The sandy layer exhibits a sharp or erosive basal contact. The whole bed is normally graded and particles are well sorted (Figs 5 and 6). Magnetic susceptibility also decreases gradually upward with a trend similar to grain size (Figs 5 and 6). In every bed, values of magnetic susceptibility are low to moderate with a mean maximum value of 600-800x10^{-5} SI, while overall the values range from 130 to

1560x10^{-5} SI. In cores KAMA21 and KAMA09, beds of Type 1 are 5-15 cm thick. When observed, from base to top, basal sandy layers consist of structureless then laminated and cross-laminated intervals. Some beds are cross-laminated only (Fig. 5). The dark clayey-silt interval exhibits alternating silty and clayey laminae (Fig. 5). Both dark and light finer-grained intervals are strongly bioturbated (Figs 5 and 6). From thin sections, the mineralogical content consists of abundant quartz, feldspar, and biotite grains and rare magnetite grains. Thin sections also revealed abundant well-preserved leaf and wood fragments trapped within the laminated and cross-laminated intervals (Fig. 5B-C). In cores KAMA10 and KAMA05, beds of Type 1 are 5-50 cm thick. They are structureless only, with abundant and scattered leaf and wood fragments.

Beds of Type 2 were mostly identified in core KAMA21 (Fig. 3). Their values of magnetic susceptibility are high with values ranging from 400 to 3270x10^{-5} SI and with a mean maximum value of 1200-1400x10^{-5} SI. They exhibit two types of facies succession:

- Type 2a consists of 10-40-cm thick well-sorted sandy beds with a sharp or erosive basal contact. Each sandy bed is normally graded but exhibits a complex grading, usually consisting of 2-5 superimposed normally graded units (Figs 7, 8, 9A). Some inversely graded units were also observed (Fig. 8). The presence of these superimposed units is also confirmed by the magnetic susceptibility (Figs 7 and 9A). The internal structure of these beds is also much more complex than in Bed-Type 1: superimposed laminated/cross-laminated units correlate with the succession of normally/inversely graded units (Figs 7 and 8). Both X-rays and thin-section images show that laminated/cross-laminated units are separated by erosive surfaces (Figs 7A-B-C, 8A-B-C). These surfaces are characterized by an increase of grain size, the accumulation of magnetite grains and the appearance/disappearance of sedimentary structures (Figs 7A-B-C, 8A-B-C). In term of mineralogy, these beds contain quartz, pyroxene, biotite. Magnetite grains, and colourless glass shards, pipe-vesicle and rounded-bubble pumices are also abundant. By comparison with beds of Type 1, they do not contain leaf and wood fragments, or very few. Several beds of Type 2a (5-10-cm thick) can be superimposed, interbedded with clayey intervals (2-3-cm thick) (Fig. 9A). In this case, sandy beds thin and fine upward. Sandwiched clayey intervals are not bioturbated.

- Type 2b is the succession of laminated silty intervals, 1-2 cm thick, interbedded with clayey layers 1-cm thick or less (Fig. 9B). Transition between two successive laminated units is marked by a thicker and coarser lamina. Then, laminae thin and fine upward in each interval. Internal truncations are observed (Fig. 9B). These intervals are never bioturbated.

Beds of Type 3 show a crude normal grading, and exhibit features of either beds of Type 1 or Type 2 regarding leaf/wood fragments and values of magnetic susceptibility. From X-ray images, the main difference with beds of Type 1 and Type 2 comes from their internal structure, as beds of Type 3 mainly consist of convolute-like structures and potential fluid-escaping structures (Fig. 10). Bioturbation is never observed in the overlying clayey intervals. Such beds were identified in cores KAMA21 and KAMA05 (Fig. 2).

Beds of Type 4 consist of well-rounded mud clasts, 2-5 cm in diameter, supported in a silty-clayey matrix (Fig. 11). The clay and silt contents are 15% and 50% on average, respectively. The matrix is fining up but with a serrated pattern showing superimposed normally- and inversely-graded intervals also revealed by the magnetic susceptibility (Fig. 11). The beds are 20-50 cm thick, with sharp basal and upper contacts. They were identified in core KAMA05 and one time in the first (top) section of KAMA21 (Fig. 3).

7. Discussion

The interest in lake deposits as archives for paleo-earthquakes has been demonstrated for many years in tectonically-controlled areas. The main evidence of past seismic shocks is the presence of post-depositional multi-scale deformation structures (Sims, 1973; Lignier et al., 1998; Monecke et al., 2004; Moernaut et al., 2009). In lakes, earthquakes are also responsible for the triggering of subaqueous failures leading to the deposition of extensive "megaturbidites" (Fanetti et al., 2008; Waldmann et al., 2011; Petersen et al., 2014; Van daele et al., 2015). These earthquake-triggered gravity deposits do not exhibit specific sedimentological features that could help discriminating them from gravity-triggered mass-wasting events (Girardclos et al., 2007). In marine environments, the synchronous emplacement of turbidites along a continental margin over hundreds of km and their correlation with historical earthquakes are still the main evidences used to identify earthquake-triggered mass-wasting events (Goldfinger et al., 2003; Sari and Cagatay, 2006; Gutiérrez-Pastor et al., 2009; Gràcia et al., 2010). Although amalgamated beds have been reported to indicate an earthquake-triggered origin (Nakajima and Kanai, 2000; Noda et al., 2008; Hassoun et al., 2014), robust sedimentological criteria to identify them as such are still lacking. The following paragraphs will discuss some criteria that could provide a preliminary step in the clear identification of earthquake-triggered turbidites along continental margins,

and set up several constrains required to potentially record these events in the sedimentary archives of a subduction trench.

7.1. 20th Century large to great subduction earthquakes recorded in the Esmeraldas Turbidite System and the prime role of the Esmeraldas Canyon

Based on the age model obtained from the upper part of core KAMA21 (Fig. 4), we correlated the four coarser-grained beds (B1-B4) to the time period of the 20th Century earthquakes (Fig. 4). Bed B4 that consists of at least two superimposed sandy units (Fig. 7) is interpreted as a bed of Type 2a, and correlated with the 1906 earthquake. Bed B3 has a strong density on the X-rays image that prevents any observation of its internal structure (Fig. 4), except convolutes in its upper part. Because B3 consists of two superimposed normally-graded sandy units, it is then interpreted as a bed of Type 2a and correlated in time with the 1942 earthquake. Bed B2 was shifted by about 20° and was probably reworked during coring (Fig. 4). It is thus impossible to interpret properly its process of deposition, but it could be correlated with the 1958 earthquake. Bed B1 consists of a thin turbidite of Type 2 overlain by a bed of Type 4 and could correlate with the 1979 earthquake. Features described in the bed of Type 4 are classically related to debris-flow deposits (Tripsanas et al., 2008; Ducassou et al., 2013). Such deposits are uncommon on turbidite levees and, in that case, should result from a local destabilisation of the superficial levee deposits during aftershock events.

So beds B4, B3, B2 and B1 found in the proximal area of the ETS could correlate with earthquakes of magnitudes from 8.8 (1906), 7.8 (1942), 7.7 (1958) and 8.2 (1979), respectively. Record of these earthquakes was not found in the distal settings of the ETS (cores KAMA10, KAMA09 and KAMA05) where mostly no 20th Century sedimentation was found, as well as in small trench basins located further south of the Esmeraldas Canyon mouth (Ratzov et al., 2010). Assuming no loss of uppermost sediment during coring, this result suggests that the 20th Century earthquakes only affected sediments located within or in the immediate vicinity of the Esmeraldas Canyon although the rupture zone of the 1906 earthquake extended along a 500-km-long segment of the margin, and the one of the 1979 earthquake is centred on the Patia Canyon (Fig. 1). The presence of natural dams (gliding masses) along the Patia Canyon is also known to block the recent sedimentation in the middle reach of the thalweg (Ratzov et al., 2012) while no obstacles exist along the Esmeraldas Canyon. The resultant earthquake-triggered gravity flows were thus trapped by the

Esmeraldas Canyon and delivered down-slope to the ETS, whereas no major synchronous lateral flows were directly generated from the open continental slope between the two Esmeraldas and Patia Canyons and likely further north. This interpretation assigns a predominant role to Esmeraldas-Canyon type (no obstacle and very steep slopes) as a collector and major venue for earthquake-triggered flows, as well as the associated proximal turbidite system.

Bed B4 associated to the 1906 earthquake of the highest magnitude is the thickest and the coarsest of the four beds identified in the 20th Century time span. The turbidite part of bed B1 associated to the 1979 earthquake, the second higher-magnitude event, is thinner and finer than bed B3 associated to the 1942 earthquake, the third higher-magnitude event. Thus factors other than the earthquake's magnitude must control both the thickness and grain size of turbidites, as already emphasized by Masson et al. (2011) on the Portuguese margin. Considering the location of the rupture zone of both the 1942 and 1979 earthquakes, the northern limit of the former is adjacent to the southern side of the Esmeraldas Canyon while the southern bound of the latter is located about 80 km northward of the Canyon (Fig. 1). The location of the earthquake relative to the area where sediments are prone to destabilize could thus influence the size of earthquake-induced turbidites.

7.2. Discrimination of earthquake-triggered deposits and their interpretation

The common features of beds of Types 1, 2 and 3 previously described, such as their good sorting, the normal grading, and the presence of sedimentary structures, indicate that they were deposited by waning turbulent flows, such as turbidity currents (Komar, 1985; Migeon et al., 2001; Mulder and Alexander, 2001). Specific features of each Type are interpreted as differences in the origin of processes that triggered turbulent flows or in post-depositional reworking of the beds.

Abundant and well-preserved leaf and wood fragments are only observed in beds of Type 1. If they originated from the erosion of organic-matter-rich deposits located within the thalweg of the canyon, all the sandy beds should exhibit a high content in such fragments, which is not the case. Their presence in beds of Type 1 thus suggests a rapid and direct transfer from land to the trench. These beds are thus thought to be deposited by currents generated at the mouth of the Esmeraldas River during high-magnitude floods. The vertical organization of structures in these beds can be classically interpreted as the Bouma sequence in turbidites (Bouma,

1962; Walker, 1967; Middleton, 1993; Migeon et al., 2001), resulting from the progressive decrease in flow regime combined with the increasing traction at the seabed. Deposition from suspension was always long enough to lead to ideal turbidite beds, implying that the parental flows persisted during a period of weeks or more, supporting the interpretation of currents generated during floods (Mulder et al., 2003) by opposition with short-lived density surges (Laval et al., 1988; Mulder and Alexander, 2001). Beds of Type 1 are thus interpreted as "classical" turbidites. The strong intensity of bioturbation observed at the top of these beds evidences an absence of sediment supply during at least several months between two successive flow events (Migeon et al., 2004).

Beds of Type 2 consist of superimposed or amalgamated sandy units. Within a single bed, each unit is characterized by a basal erosive surface associated with a sharp change in both grain size and mineral composition, a normal grading (rarely inverse grading), and laminations and/or cross-laminations. Each unit is thus interpreted to be deposited by a single turbulent flow, so a single bed-Type 2 should result from deposition by multiple quasi-synchronous flows. Similar amalgamated sandy beds were already described on the eastern and western margin of the Hokkaido/Honshu Islands (Nakajima and Kanai, 2000; Noda et al., 2008), along the Cascadia margin (Goldfinger et al., 2008; Gutiérrez-Pastor et al., 2013), along the Sumatra-Andaman subduction zone (Patton et al., 2015), and in the Ligurian basin (Hassoun et al., 2014). In these cases, they have been interpreted as turbidites linked with major earthquakes. In the Colombia Trench, the temporal correlation between bed-Type 2 B3 and B4 and the 1942 and 1906 earthquakes supports such interpretation. Although amalgamation appears as a robust criterion characterizing earthquake-induced turbidites, simple graded beds have been also reported to be earthquake-induced at sea (Gutiérrez-Pastor et al., 2013; Patton et al., 2015; Ratzov et al., 2015), in fjords (St-Onge et al., 2012) and in lakes (Moernaut et al., 2014). In these cases, factors like type of seismic rupture, intensity of ground acceleration, distance from coring sites to epicentres, presence/absence of channelizing structures should be further investigated to explain differences in the deposit features. In the Colombia Trench, in addition to the amalgamation criteria, the absence of leaf and wood fragments but the abundance of ferromagnesian minerals together with pumices in beds of Type 2 show a source area that differs from that of Type 1-beds and support reworking of volcanoclastic-rich submarine-slope deposits by landslides. Such volcanoclastic deposits exist as 10-20-cm thick tephra layers on the continental slope along the margin (Ratzov, 2009). So, Type 2-beds are interpreted to result from the quasi-simultaneous

deposition by several gravity flows triggered synchronously in a limited region of the active margin during a single seismic shock.

When considering several superimposed beds of Type 2a (Fig. 9A) or single beds of Type 2b (Fig. 9B), coarser-grained intervals are interbedded with non-bioturbated clayey intervals related to the decantation of the dilute part of turbulent flows (Stow and Piper, 1984). Time deposition of such fine-grained intervals few centimetre thick can be as short as few hours, as evidenced on levees of the Zaïre turbidite system (Migeon et al., 2004). Without evidence of erosion at the base of the overlying sandy beds, the absence of bioturbation cannot be explained by seafloor erosion. In addition, when present, bioturbated hemipelagic intervals 2-3 cm thick were evidenced on top of classical turbidite beds. It suggests that time period between the deposition of two successive Type 2a-beds or clayey-silty laminated intervals in Type 2b was too short, i.e. less than few weeks or months, to allow the benthic fauna to re-colonize the seafloor. Such rapid succession of events in a tectonically-active area like the Colombia Trench could evidence the impact of several successive major earthquake shocks. In that case, the fining/thinning-up pattern could illustrate the wash-out of the softer sediment reservoir on the continental slope by the first shocks, the remaining slope sediment being more indurated and more difficult to destabilize by the following shocks which leads to a decrease of volume and grain size of particles transported to the trench.

Beds of Type 3 have common features with beds of Type 1 and Type 2 and were thus deposited under similar hydrodynamic conditions but the presence of convolute-like structures and fluid-escape pipes suggest post-depositional reworking processes (Lignier et al., 1998; Rossetti, 1999; Rodriguez-Pasqua et al., 2000). Because Type 3-beds do not exhibit coring disturbances (sand flows along the liner, bed tilting), these structures cannot be artefacts. Convolutes are classically explained by liquefaction affecting sandy layers with high-water content shortly after their deposition (Sims, 1973; Monecke et al., 2004). As convolutes are present over the whole thickness of the beds, they cannot result from a simple overloading caused by the overlying deposits that are always too thin (few cm to 20 cm) to induce a strong lithostatic pressure. Instead, they more likely result from the entire liquefaction of beds that requires a stress induced by seismic shocks and ground acceleration. Beds of Type 3 are thus interpreted as pre-existing beds that were liquefied during earthquakes a short time after their deposition in the trench, or as earthquake-induced turbidites liquefied during the following aftershocks or earthquakes.

7.3. Constrains to assess the recurrence of large earthquakes on the north Ecuador/south Colombia margin

In addition to the known large-magnitude earthquakes (1906, 1942, 1958, 1979 and 2016), and their lower magnitude aftershock sequences, a number of lower magnitude earthquakes (Mw = 4-6) also affected the north Ecuador/south Colombia margin during the 20th Century (PDE catalogues; Engdahl et al., 1998) but these events were not recorded in core KAMA21. Two hypotheses could account for this observation:

- the lower-magnitude earthquakes did not trigger landslides because their peak-ground acceleration was too low to affect continental-slope deposits, or there were no continental-slope sediments available because they had already been washed out by the previous main 1906, 1942, 1958 and 1979 shocks,

- the lower-magnitude earthquakes did trigger landslides, but their volume was too small to generate thick turbulent flows through basal erosion and incorporation of ambient water. Because core KAMA21 was collected on a levee about 100 m high, the levee may have acted as a natural filter that prevented the thin (< 100-m thick) earthquake-induced turbulent flows to overflow the levee crest.

Because the Esmeraldas Canyon is directly connected to the Esmeraldas River, the canyon flanks and the neighbouring margin slope should be regularly fed with new finer-grained sediments, suggesting the second hypothesis should be favoured. Hence, only earthquakes generating the highest local shaking intensity able to trigger thick turbulent flows have probably been recorded on the turbidite levee in the region of core KAMA21. The absence of potential earthquake-induced turbidites in cores KAMA10 and KAMA05 and the presence of only one in core KAMA09 suggest that, when entering the Esmeraldas Channel, a large majority of flows were first thick enough to overflow the left-hand levee and then they died out before reaching the Lobe 1, probably through a continuous process of deposition along the channel-levee system. Another hypothesis explaining the quasi absence of earthquake-induced turbidites in Lobe 1 could be that synchronous earthquake-induced gravity flows transformed along the Esmeraldas Channel by incorporating sediment and/or by merging together, resulting in a single larger flow whose deposit will miss the amalgamated character but will consist of a thick normally-graded bed as observed in core KAMA10. Therefore, the use of earthquake-induced turbidites to evaluate the recurrence intervals of earthquakes in a

given area should be done with great precaution as the resulting paleoseismicity scale could strongly depend on the location of the cores with respect to the local trench morphology.

7.4. Recurrence of large earthquakes on the north Ecuador/south Colombia margin

Based on the previous considerations, only earthquakes with magnitude greater than 7.7 were recorded in the levee deposits of the ETS during the 20th Century. Thus the earthquake recurrence that can be deduced from the sediment record in core KAMA21 should concern earthquakes with magnitude greater than 7-8. In addition to beds B1 to B4, six earthquake-triggered turbidites (bed-Type 2; Fig. 3) identified between 130 and 550 cm depth could be associated with earthquakes of such range of magnitude.

In core KAMA21, an age model was deduced from the hemipelagic sedimentation rates estimated using both excess activity of ^{210}Pb and the two ^{14}C dates. The hemipelagic muddy intervals were recognized from their light colour on X-rays images. The transition between the muddy turbidite intervals and the overlying muddy hemipelagites was not always clearly identified because of the bioturbation. In this case, one considered an interval of confidence plus an interval of uncertainty of a few millimetres to a few centimetres thick. The first core interval separating the 1906 turbidite (B4) from the preceding earthquake-induced turbidite (B5) comprises 45 cm (+ 11 cm of uncertainty) of hemipelagic muds, corresponding to a recurrence time of 268 ± 27 yrs. Going downcore, the five preceding earthquake-induced turbidites are separated on average by 15-23 cm (+ 6 cm of uncertainty) of hemipelagic muds, corresponding to recurrence times of 42-82 ± 30 yrs. By comparison, recurrence time for the turbidites of Type 1 is about 5-10 years, matching the El Nino periodicity (Moy et al., 2002) and supporting our interpretation of deposits related to flood-generated currents.

Since the beginning of the 20th Century, considering similar fault segments, recurrence times are 36, 52 and 73 years for the 1942, 1958 and 1979 events respectively after the great 1906 earthquake, and it is of 74 years between the 1942 and 2016 earthquakes. Based on GPS measurements and an estimation of the seismic moment deficit rate in every rupture area of the 20th Century earthquakes, Chlieh et al. (2014) proposed that earthquakes such as those in 1942, 1958 and 1979 could rupture their seismic asperity with characteristic recurrence times of 140 ± 30 years, 90 ± 20 years, 153 ± 80 years respectively. Except for one time interval (B4-B5), recurrences determined in this study from the paleoseismology of turbidites are shorter than those given above, considering the rupture of the full fault segment (1906) and

those of each individual rupture segments (1942, 1958, 1979) to have generated earthquake-induced turbidites found at site KAMA21. This suggests that earthquakes with magnitude greater than 7 could be more common than previously estimated by Chlieh et al. (2014). Recurrences estimated in this study strongly depend on the accuracy of the hemipelagic sedimentation rates. Calculation uncertainties could explain the differences in recurrences estimated in these two studies. Anyway, without testimonies reporting about the seismic activity, our results suggest that large earthquakes regularly affected the north Ecuador/south Colombia margin during historical times.

An important question that stems from these results is the possibility that a great earthquake similar to the 1906 event had occurred along the studied-margin segment during historical times. By comparison with the thickness, grain size, and internal organization of the 1906 turbidite, Type-2 beds B8 and B10 in core KAMA21 could be good candidates. Based on the age model, B8 and B10 may have deposited in AD 1385 ± 24 years and AD 1281 ± 30 years respectively. Chlieh et al. (2014) proposed a recurrence time of at least 575 ± 100 years for large 1906-type earthquakes. Both B8 and B10 are in the range of such recurrence time, supporting the likely occurrence of at least a 1906-type earthquake 600 years ago. Further investigation should thus concentrate on the recognition and dating of such an event along the north Ecuador/south Colombia margin.

8. Conclusion

The north Ecuador/south Colombia subduction trench (Pacific) is characterised by the construction of a turbidite system fed by the Esmeraldas Canyon connected to the Esmeraldas River. During the past 110 years, this area was affected by five large to great subduction earthquakes (1906, 1942, 1958, 1979, 2016). From the study of four cores collected in the trench, in both levee and lobes of the Esmeraldas Turbidite System, an attempt is made to discriminate the classical trench sedimentation from the detritic beds potentially related to the regional seismicity.

On the basis of sedimentological and mineralogical criteria, we propose to discriminate deposits of flood-generated turbidity currents from earthquake-induced turbidity currents as follows:

- classical turbidites deposited by flood-generated turbidity currents are characterized by normally-graded sandy beds, with the well-known succession of sedimentary structures

described in the so-called Bouma sequence. These beds exhibit abundant wood and leaf fragments, suggesting a rapid and direct transfer of the material from land to sea. Clayey intervals between two successive turbidites are highly bioturbated.

- earthquake-induced turbidites are characterized by silty to sandy beds with a more complex internal organisation. They consist of either single beds showing amalgamation of several normally-graded laminated/cross-laminated intervals separated by erosional surfaces, or succession of amalgamated beds with decreasing grain sizes and separated with non bioturbated clayey intervals. Leaf and wood fragments are absent but the abundance of ferromagnesian minerals and pumices suggests the reworking of continental-slope tephra deposits. Individual amalgamated beds are thought to be related to a major shock affecting a significant portion of the margin and triggering multiple landslides collected by the Esmeraldas canyon, and evolving into turbidity currents depositing quasi-synchronously their particles at similar trench locations. Succession of amalgamated beds is interpreted to result from a series of major shocks (potentially aftershocks), the fining-/thinning-up pattern being related to the wash-out of softest sediments during each shock while more indurated sediments are left on a bare seafloor and are more and more difficult to destabilize.

The impact of earthquakes on the trench sedimentation is also evidenced by the presence of convolutes and vertical fluid-escape structures in coarse-grained beds, interpreted as post-depositional reworking processes.

Age models based on ^{210}Pb in excess illustrates that sedimentation occurred during the 20th Century in the proximal levees, close to the mouth of the Esmeraldas Canyon. A temporal relationship was then established between the 1906, 1942, and 1979 major earthquakes and three coarse-grained beds showing features of earthquake-induced turbidites, suggesting the canyon flanks and surrounding areas were the main reservoir for sediments to be remobilized during earthquakes. The fining and thinning observed between the 1906, 1942 and 1979 turbidites correlate with the increasing distance of the rupture zone of each earthquake with the Esmeraldas Canyon.

During the 20th Century, earthquakes with magnitudes lower than 6-7 also affected the same margin segment but were not recorded in the proximal levee, suggesting that the turbidite levee acted as a natural filter that prevented the earthquake-induced turbidity currents thinner than ~100 m from overflowing. Age models based on both ^{210}Pb in excess and ^{14}C dating illustrate that at least ten earthquakes with the highest magnitudes were recorded on the

turbidite levee within the last 800 years with a recurrence time ranging from about 268 ± 27 yrs to 42-82 ± 30 yrs, or less for the 20th Century earthquakes. The comparison of the main features of the 1906 turbidite with older earthquake-triggered turbidites identified in a core collected in the trench suggests that one or two earthquakes similar to the 1906 event might have occurred ~600 yrs ago. Further investigations should be performed to identify, to date and to correlate such an event along the north Ecuador/south Colombia margin.

Acknowledgments

The authors thank the captain and crew of the RV L'Atalante and all the scientists and technicians who participated in the AMADEUS cruise. This work has been funded by the French program "GDR Marges" and the French "Institut pour la Recherche et le Développement" (IRD). The authors are grateful to Marc De Batist and to the two anonymous reviewers for their constructive comments and suggestions. ^{14}C dating was performed by Beta Analytic.

References

Avsar, U., Hubert-Ferrari, A., De Batist, M., Lepoint, L., Schmidt, S., Fagel, N., 2014. Seismically-triggered organic-rich layers in recent sediments from Göllükoy Lake (North Anatolian Fault, Turkey). Quaternary Science Reviews 103, 67-80.

Beck, C., Mercier de Lepinay, B., Schneider, J.-L., Cremer, M., Cagatay, N., Wendenbaum, E., Boutareaud, S., Ménot, G., Schmidt, S., Weber, O., Eris, K., Armijo, R., Meyer, B., Pondard, N., Gutscher, M.-A., the Marmacore Cruise Party, 2007. Late Quaternary co-seismic sedimentation in the Sea of Marmara's deep basins. Sedimentary Geology 199, 65-89.

Beck, S.L., Ruff, L.J., 1984. The rupture process of the great 1979 Colombia earthquake: evidence for the asperity model. Journal of Geophysical Research 89, 9281-9291.

Becker, A., Ferry, M., Monecke, K., Schnellmann, M., Giardini, D., 2005. Multiarchive paleoseismic record of late Pleistocene and Holocene strong earthquakes in Switzerland. Tectonophysics 400, 153-177.

Bouma, A.H., 1962. Sedimentology of some flysch deposits: a graphic approach to facies interpretation. Elsevier, Amsterdam.

Chapron, E., Beck, C., Pourchet, M., Deconinck, J.-F., 1999. 1822 earthquake-triggered homogenite in Lake Le Bourget (NW Alps). Terra Nova 11, 86-92.

Chlieh, M., Mothes, P.A., Nocquet, J.-M., Jarrin, P., Charvis, P., Cisneros, D., Font, Y., Collot, J.-Y., Villegas-Lanza, J.-C., Rolandone, F., Vallée, M., Regnier, M., Segovia, M., Martin, X., Yepes, H., 2014. Distribution of discrete seismic asperities and aseismic slip along the Ecuadorian megathrust. Earth and Planetary Science Letters 400, 292-301.

Collot, J.-Y., Agudelo, W., Ribodetti, A., Marcaillou, B., 2008. Origin of a crustal splay fault and its relation to the seismogenic zone and underplating at the erosional N-Ecuador S-Columbia oceanic margin. Journal of Geophysical Research 113.

Collot, J.-Y., Marcaillou, B., Sage, F., Michaud, F., Agudelo, W., Charvis, P., Graindorge, D., Gutscher, M.-A., Spence, G., 2004. Are rupture zone limits of great subduction earthquakes controlled by upper plate structures? Evidence from multichannel seismic reflection data acquired across the northern Ecuador-southwest Colombia margin. Journal of Geophysical Research 109.

Collot, J.-Y., Migeon, S., Spence, G., Le Gonidec, Y., Marcaillou, B., Schneider, J.-L., Michaud, F., Alvarado, A., Lebrun, J.-F., Sosson, M., Pazmino, A., 2005. Seafloor margin map helps in understanding subduction earthquakes. Eos 86, 463-465.

Ducassou, E., Migeon, S., Capotondi, L., Mascle, J., 2013. Run-out distance and erosion of debris flows in the Nile deep-sea fan system: Evidence from lithofacies and micropalaeontological analyses. Marine and Petroleum Geology 39, 102-123.

Engdahl, E.R., Van der Hilst, R.P., Buland, R.P., 1998. Global teleseismic earthquake relocation with improved travel times and procedures for depth determination. Bulletin of the Seismological Society of America 88, 722-743.

Fanetti, D., Anselmetti, F.S., Chapron, E., Sturm, M., Vezzoli, L., 2008. Megaturbidite deposits in the Holocene basin fill of lake Como (Southern Alps, Italy). Palaeogeography, Palaeoclimatology, Palaeoecology 259, 323-340.

Girardclos, S., Schimdt, O.T., Sturm, M., Ariztegui, D., Pugin, A., Anselmetti, F.S., 2007. The 1996 AD delta collapse and large turbidite in Lake Brienz. Marine Geology 241, 137-154.

Goldfinger, C., 2011. Submarine paleoseismology based on turbidite records. Annual Review of Marine Science 3, 36-66.

Goldfinger, C., Grijalva, K., Burgmann, R., Morey, A.E., Johnson, J.E., Hans Nelson, C., Gutiérrez-Pastor, J., Ericsson, A., Karabanov, E., Chaytor, J.D., Patton, J.R., Gràcia, E., 2008. Late Holocene rupture of the Northern San Andreas Fault and possible stress linkage to the Cascadia Subduction Zone. Bulletin of the Seismological Society of America 98, 861-889.

Goldfinger, C., Nelson, C.H., Johnson, J.E., the Shipboard Scientific Party, 2003. Deep-water turbidites as Holocene earthquake proxies: the Cascadia subduction zone and Northern San Andreas Fault systems. Annals of Geophysics 46, 1169-1194.

Gorsline, D.S., De Diego, T., Nava-Sanchez, E.H., 2000. Seismically triggered turbidites in small margin basins: Alfonso Basin, Western Gulf of California and Santa Monica Basin, California Borderland. Sedimentary Geology 135, 21-35.

Gràcia, E., Vizcaino, A., Escutia, C., Asioli, A., Rodès, A., Pallàs, R., Garcia-Orellana, J., Lebreiro, S., Goldfinger, C., 2010. Holocene earthquake record offshore Portugal (SW Iberia): testing turbidite paleosseismicity in a slow-convergence margin. Quaternary Science Reviews 29, 1156-1172.

Gutiérrez-Pastor, J., Nelson, C.H., Goldfinger, C., Escutia, C., 2013. Sedimentology of seismo-turbidites off the Cascadia and northern California active tectonic continental margins, northwest Pacific Ocean. Marine Geology 336, 99-119.

Gutiérrez-Pastor, J., Nelson, C.H., Goldfinger, C., Johnson, J.E., Escutia, C., Eriksson, A., Morey, A.E., Party, T.S.S., 2009. Earthquake control of Holocene turbidite frequency confirmed by hemipelagic sedimentation chronology on the Cascadia and northern California active continental margins, External Controls on Deep-Water Depositional Systems. SEPM Special Publication, pp. 179-197.

Hassoun, V., Martin, J., Migeon, S., Larroque, C., Cattaneo, A., Eriksson, M., Sanchez-Cabeza, J.A., Mercier de Lepinay, B., Liong Wee Kwong, L., Levy, I., Heimburger, L.-E., Miquel, J.-C., 2014. Searching for the record of historical earthquakes, floods and anthropogenic activities in the Var Sedimentary Ridge (NW Mediterranean), in: Krastel, S., Behrmann, J.-H., Völker, D., Stipp, M., Berndt, C., Urgeles, R., Chaytor, J.D., Huhn,

K., Strasser, M., Harbitz, C.B. (Eds.), Submarine Mass Movements and Their Consequences. Springer International Publishing, Switzerland, pp. 571-581.

Huh, C.-A., Su, C.-C., Liang, W.-T., Ling, C.-Y., 2004. Linkages between turbidites in the southern Okinawa Trough and submarine earthquakes. Geophysical Research Letters 31, doi:10.1029/2004GL019731.

Huh, C.-A., Su, C.-C., Wang, C.-H., Lee, S.-Y., Lin, I.-T., 2006. Sedimentation in the Southern Okinawa trough - Rates, turbidites and a sediment budget. Marine Geology 231, 129-139.

Kanamori, H., Given, J.W., 1981. Use of long-period surface waves for rapid determination of earthquake source parameters. Physics of the Earth and Planetary Interiors 27, 8-31.

Kelleher, J., 1972. Rupture zones of large South American earthquakes and some predictions. Journal of Geophysical Research 77, 2087-2103.

Kempf, P., Moernaut, J., Van Daele, M., Vermassen, F., Vandoorne, W., Pino, M., Urrutia, R., Schimdt, S., Garrett, E., De Batist, M., 2015. The sedimentary record of the 1960 tsunami in two coastal lakes on Isla de Chiloé, south central Chile. Sedimentary Geology 328, 73-86.

Kenyon, N.H., Klaucke, I., Millington, J., Ivanov, M.K., 2002. Sandy submarine canyon-mouth lobes on the western margin of Corsica and Sardinia, Mediterranean Sea. Marine Geology 184, 69-84.

Kirchner, G., 2011. ^{210}Pb as a tool for establishing sediment chronologies: examples of potentials and limitations of conventianal dating models. Journal of Environemental Radioactivity 102, 490-494.

Komar, P.D., 1985. The hydraulic interpretation of turbidites from their grain sizes and sedimentary structures. Sedimentology 32, 395-407.

Laval, A., Cremer, M., Beghin, P., Ravenne, C., 1988. Density surges: two-dimensional experiments. Sedimentology 35, 73-84.

Lignier, V., Beck, C., Chapron, E., 1998. Caractérisation géométrique et texturale de perturbations synsédimentaires attribuées à des séismes, dans une formation quaternaire glaciolacustre des Alpes ("les Argiles du Trièves"). Comptes Rendus de l'Académie des Sciences Paris 327, 645-652.

Lonsdale, P., 2005. Creation of the Cocos and Nazca plates by fission of the farallon plate. Tectonophysics 404, 237-264.

Maslin, M., Vilela, C., Mikkelsen, N., Grootes, P., 2005. Causes of catastrophic sediment failures of the Amazon Fan. Quaternary Science Reviews 24, 2180-2193.

Masson, D.G., Arzola, R.G., Wynn, R.B., Hunt, J.E., Weaver, P.P.E., 2011. Seismic triggering of landslides and turbidity currents offshore Portugal. Geochemistry, Geophysics, Geosystems 12, 1-19.

Mendoza, C., Dewey, J.W., 1984. Seismicity associated with the great Colombia-Ecuador earthquakes of 1942, 1958 and 1979: implications for barrier models of earthquake rupture. Bulletin of the Seismological Society of America 74, 577-593.

Middleton, G.V., 1993. Sediment deposition from turbidity currents. Annual Review of Earth and Planetary Sciences 21, 89-114.

Migeon, S., Ducassou, E., Le Gonidec, Y., Rouillard, P., Mascle, J., Revel-Rolland, M., 2010. Lobe construction and sand/mud segregation by turbidity currents and debris flows on the western Nile deep-sea fan (Eastern Mediterranean). Sedimentary Geology 229, 124-143.

Migeon, S., Savoye, B., Babonneau, N., Spy-Andersson, F.-L., 2004. Processes of sediment-wave construction along the present Zaire deep-sea meandering channel: role of meanders and flow-stripping. Journal of Sedimentary Research 74, 580-598.

Migeon, S., Savoye, B., Faugères, J.-C., 2000. Quaternary development of migrating sediment waves in the Var deep-sea fan: distribution, growth pattern, and implication for levee evolution. Sedimentary Geology 133, 265-293.

Migeon, S., Savoye, B., Zanella, E., Mulder, T., Faugères, J.-C., Weber, O., 2001. Detailed seismic-reflection and sedimentary study of turbidite sediment waves on the Var Sedimentary Ridge (SE France): significance for sediment transport and deposition and for the mechanisms of sediment-wave construction. Marine and Petroleum Geology 18, 179-208.

Migeon, S., Weber, O., Faugères, J.-C., Saint-Paul, J., 1999. SCOPIX: a new X-ray imaging system for core analysis. Geo-Marine Letters 18, 251-255.

Moernaut, J., De Batist, M., Charlet, F., Heirman, K., Chapron, E., Pino, M., Brümmer, R., Urrutia, R., 2007. Giant earthquakes in South-Central Chile revealed by Holocene mass-wasting events in Lake Puyehue. Sedimentary Geology 195, 239-256.

Moernaut, J., De Batist, M., Heirman, K., Van Daele, M., Pino, M., Brümmer, R., Urrutia, R., 2009. Fluidization of buried mass-wasting deposits in lake sediments nd its relevance for paleoseismology: Results from a reflection seismic study of lakes Villarrica and Clafquén (South-Central Chile). Sedimentary Geology 213, 121-135.

Moernaut, J., Van Daele, M., Heirman, K., Fontijn, K., Strasser, M., Pino, M., Urrutia, R., De Batist, M., 2014. Lacustrine turbidites as tool for quantitative earthquake reconstruction: New evidence for a variable rupture mode in south central Chile. Journal of Geophysical Research: Solid Earth 119, 1607-1633.

Monecke, K., Anselmetti, F.S., Becker, A., Sturm, M., Giardini, D., 2004. The record of historic earthquakes in lake sediments of Central Switzerland. Tectonophysics 394, 21-40.

Moy, C.M., Seltzer, G.O., Rodbell, D.T., Anderson, D.M., 2002. Variability of El Nino/Southern Oscillation activity at millennial timescales during the Holocene epoch. Nature 420, 162-165.

Mulder, T., Alexander, J., 2001. The physical character of subaqueous sedimentary density flows and their deposits. Sedimentology 48, 269-299.

Mulder, T., Migeon, S., Savoye, B., Jouanneau, J.-M., 2001a. Twentieth century floods recorded in the deep Mediterranean sediments. Geology 29, 1011-1014.

Mulder, T., Syvitski, J.P.M., Migeon, S., Faugères, J.-C., Savoye, B., 2003. Marine hyperpycnal flows: initiation, behavior and related deposits. A review. Marine and Petroleum Geology 20, 861-882.

Mulder, T., Weber, O., Anschutz, P., Jorissen, F., Jouanneau, J.-M., 2001b. A few months-old storm-generated turbidite deposited in the Capbreton Canyon (Bay of Biscay, SW France). Geo-Marine Letters 21, 149-156.

Nakajima, T., Kanai, Y., 2000. Sedimentary features of seismoturbidites triggered by the 1983 and older historical earthquakes in the eastern margin of the Japan Sea. Sedimentary Geology 135, 1-19.

Nelson, A.R., Kelsey, H.M., Witter, R.C., 2006. Great earthquakes of variable magnitude at the Cascadia subduction zone. Quaternary Research 65, 345-365.

Nocquet, J.-M., Villegas-Lanza, J.-C., Chlieh, M., Mothes, P.A., Rolandone, F., Jarrin, P., Cisneros, D., Alvarado, A., Audin, L., Bondoux, F., Martin, X., Font, Y., Regnier, M., Vallée, M., Tran, T., Beauval, C., Maguina Mendoza, J.M., Martinez, W., Tavera, H., Yepes, H., 2014. Motion of continental slivers and creeping subduction in the northern Andes. Nature Geoscience 7, 287-291.

Noda, A., TuZino, T., Kanai, Y., Furukawa, R., Uchida, J., 2008. Paleoseismicity along the southern Kuril Trench deduced from submarine-fan turbidites. Marine Geology 254, 73-90.

Normark, W.R., Piper, D.J.W., Posamentier, H., Pirmez, C., Migeon, S., 2002. Variability in form and growth of sediment waves on turbidite channel levees. Marine Geology 192, 23-58.

Patton, J.R., Goldfinger, C., Morey, A.E., Ikehara, K., Romsos, C., Stoner, J.S., Djadjadihardja, Y., Udrekh, Ardhyastuti, S., Gaffar, E.Z., Vizcaino, A., 2015. A 6600 year earthquake history in the region of the 2004 Sumatra-Andaman subduction zone earthquake. Geosphere 11, 2067-2129.

Petersen, J., Wilhelm, B., Revel, M., Rolland, Y., Crouzet, C., Arnaud, F., Brisset, E., Chaumillon, E., Magand, O., 2014. Sediments of Lake Vens (SW European Alps, France) record large-magnitude earthquake events. Journal of Paleolimnology 51, 343-355.

Piper, D.J.W., Normark, W.R., 2009. Processes that initiate turbidity currents and their influence on turbidites: a marine geology perspective. Journal of Sedimentary Research 79, 347-362.

Polonia, A., Panieri, G., Gasperini, L., Gasparotto, G., Bellucci, L.G., Torelli, L., 2013. Turbidite paleoseismology in the Calabrian Arc Subduction Complex (Ionian Sea). Geochemistry, Geophysics, Geosystems 14, 112-140.

Pouderoux, H., Proust, J.-N., Lamarche, G., 2015. Submarine paleoseismology of the northern Hikurangi subduction margin of New Zealand as deduced from turbidite record since 16 ka. Quaternary Science Reviews 84, 116-131.

Ratzov, G., 2009. Processus gravitaires sous-marins le long de la zone de subduction Nord Equateur - Sud Colombie : Apports à la connaissance de l'érosion tectonique et de la déformation d'une marge active et implications sur la genèse de tsunamis. University of Nice Sophia Antipolis, Nice, p. 246.

Ratzov, G., Cattaneo, A., Babonneau, N., Déverchère, J., Yelles, K., Bracène, R., Courboulex, F., 2015. Holocene turbidites record earthquake supercycles at a slow-rate plate boundary. Geology 43, 331-334.

Ratzov, G., Sosson, M., Collot, J.-Y., Migeon, S., 2012. Late Quaternary geomorpholgic evolution of submarine canyons as a marker of active deformation on convergent margins: the example of the south Colombian margin. Marine Geology 315-318, 77-97.

Ratzov, G., Sosson, M., Collot, J.-Y., Migeon, S., Michaud, F., Lopez, E., Le Gonidec, Y., 2007. Submarine landslides along the North Ecuador-South Colombia convergent margin: possible tectonic control, in: Lykousis, V., Sakellariou, D., Locat, J. (Eds.), Submarine Mass Movements and Their Consequences. Springer, pp. 47-55.

Robbins, J.A., Eglington, D.N., 1975. Determination of recent sedimentation rates in Lake Michigan using Pb-210 and Cs-137. Geochimica et Cosmochimica Acta 39, 285-304.

Rodriguez-Pasqua, M.A., Calvo, J.P., De Vicente, G., Gomez-Gras, D., 2000. Soft-sediment deformation structures interpreted as seismites in lacustrine sediments of the Prebetic Zone, SE Spain, and their potential use as indicators of earthquake magnitudes during the Late Miocene. Sedimentary Geology 135, 117-135.

Rossetti, D.d.F., 1999. Soft-sediment deformation structures in late Albian to Cenomanian deposits, São Luis Basin, northern Brazil: evidence for palaeoseismicity. Sedimentology 46, 1065-1081.

Sari, E., Cagatay, N., 2006. Turbidites and their association with past earthquakes in the deep Cinarcik Basin of the Marmara Sea. Geo-Marine Letters 26, 69-76.

Schmidt, S., De Deckker, P., 2015. Present-day sedimentation rates on the southern and southeastern Australian continental margins. Australian Journal of Earth Sciences 62, 143-150.

Schnellmann, M., Anselmetti, F.S., Giardini, D., McKenzie, J.A., Ward, S.N., 2002. Prehistoric earthquake history revealed by lacustrine slump deposits. Geology 30, 1131-1134.

Schwab, W.C., Lee, H.J., Twichell, D.C., Locat, J., Nelson, C.H., McArthur, W.G., Kenyon, N.H., 1996. Sediment mass-flow processes on a depositional lobe, outer Mississippi Fan. Journal of Sedimentary Research 66, 916-927.

Shiki, T., Kumon, F., Inouchi, Y., Kontani, Y., Sakamoto, T., Tateishi, M., Matsubara, H., Fukuyama, K., 2000. Sedimentary features of the seismo-turbidites, Lake Biwa, Japan. Sedimentary Geology 135, 37-50.

Sims, J.D., 1973. Earthquake-induced structures in sediments of Van Norman Lake, San Fernando, California. Science 182, 161-163.

Sims, J.D., 1975. Determining earthquake recurrence intervals from deformational structures in young lacustrine sediments. Tectonophysics 29.

Smoot, J.P., Litwin, R.J., Bischoff, J.L., Lund, S.J., 2000. Sedimentary record of the 1872 earthquake and "Tsunami" at Owens Lake, southeast California. Sedimentary Geology 135, 241-254.

St-Onge, G., Chapron, E., Mulsow, S., Salas, M., Viel, M., Debret, M., Foucher, A., Mulder, T., Winiarski, T., Desmet, M., Costa, P.J.M., Ghaled, B., Jaouen, A., Locat, J., 2012. Comparison of earthquake-triggered turbidites from the Saguenay (Eastern Canada) and Reloncavi (Chilean margin) Fjords: Implications for paleoseismicity and sedimentology. Sedimentary Geology 243-244, 89-107.

St-Onge, G., Mulder, T., Piper, D.J.W., Hillaire-Marcel, C., Stoner, J.S., 2004. Earthquake and flood-induced turbidites in the Saguenay Fjord (Québec): a Holocene paleoseismicity record. Quaternary Science Reviews 23, 283-294.

Stow, D.A.V., Piper, D.J.W., 1984. Deep-water fine-grained sediments: facies models, in: Stow, D.A.V., Piper, D.J.W. (Eds.), Fine-Grained Sediments: Deep-Water Processes and Facies. Geological Society London, Special Publication, pp. 611-646.

Subarya, C., Chlieh, M., Prawirodirdjo, L., Avouac, J.-P., Bock, Y., Sieh, K., Meltzner, A.J., Natawidjaja, D.H., McCaffrey, R., 2006. Plate-boundary deformation associated with the great Sumatra-Andaman earthquake. Nature 440, 46-51.

Swenson, J.L., Beck, S.L., 1996. Historical 1942 Ecuador and 1942 Peru subduction earthquakes, and earthquake cycles along Colombia-Ecuador and Peru subduction segments. Pageoph. 146, 67-101.

Tripsanas, E., Piper, D.J.W., Jenner, K.A., Bryant, W.R., 2008. Submarine mass-transport facies: new perspectives on flow processes from cores on the eastern North American margin. Sedimentology 55, 97-136.

Unterseh, S., Cochonat, P., Voisset, M., Ollier, G., Harmegnies, F., 1998. Acoustic data ground truthing through in-situ measurements of physical properties, International Offshose and Polar Engineering Conference (ISOPE). ISOP, Montreal, Canada, pp. 689-692.

Van Daele, M., Moernaut, J., Doom, L., Boes, E., Fontijn, K., Heirman, K., Vandoorne, W., Hebbeln, D., Pino, M., Urrutia, R., Brümmer, R., De Batist, M., 2015. A comparison of the sedimentary records of the 1960 and 2010 great Chilean earthquakes in 17 lakes: Implcations for quantitative lacustrine palaeoseismology. Sedimentology 62, 1466-1496.

Vanneste, K., Meghraoui, M., Camelbeeck, T., 1999. Late Quaternary earthquake-related soft-sediment deformation along the Belgian portion of the Feldbiss Fault, Lower Rhine Graben system. Tectonophysics 309, 57-79.

Waldmann, N., Anselmetti, F.S., Ariztegui, D., Austin, J.A., Pirouz, M., Moy, C.M., Dunbar, R., 2011. Holocene mass-wasting events in Lago Fagnano, Tierra del Fuego (54°S): implications for paleoseismicity of the Magallanes-fagnano transform fault. Basin Research 23, 171-190.

Walker, R.G., 1967. Turbidite sedimentary structures and their relationship to proximal and distal depositional environments. Journal of Sedimentary Petrology 37, 25-43.

Zaragosi, S., Auffret, G.A., Faugères, J.-C., Garlan, T., Pujol, C., Cortijo, E., 2000. Physiography and recent sediment distribution of the Celtic Deep-Sea Fan, Bay of Biscay. Marine Geology 169, 207-237.

Zaragosi, S., Bourillet, J.-F., Eynaud, F., Toucanne, S., Denhard, B., Van Toer, A., Lanfumey, V., 2006. The impact of the last European deglaciation on the deep-sea turbidite systems of the Celtic-Armorican margin (Bay of Biscay). Geo-Marine Letters 26, 317-329.

Figure caption

Figure 1: Shaded bathymetric map illustrating the morphology of the north Ecuador/south Colombia margin after the AMADEUS cruise (Collot et al., 2005). The white dashed lines follow the contour of the main scars located along the Esmeraldas Canyon and on the continental slope. EC1 and EC2 are the first and second segment of the Esmeraldas Channel, respectively. Red dots are the location of cores shown in Figure 2. Inset A illustrates the location of the study area (red square) along the north Ecuador/south Colombia margin. Inset B indicates the locations (star), rupture zones (white dashed-line) and focal mechanisms (beach ball) of the main earthquakes that affected the margin during the 20th Century together with their aftershock sequences (dots) (adapted from Collot et al., 2004). Black thick lines are main interpreted faults and barbed-line is the deformation front. The blue-dashed frame is the study area. Inset C and D illustrate the backscatter acoustic facies associated with Lobe 1 and 2.

Figure 2: Chirp profile collected across the right-hand levee and Lobe 1 of the ETS. Levee is characterized by a well-layered echofacies with wavy structures interpreted as sediment waves. Lobe 1 exhibits a strong seafloor reflection with no or little penetration suggesting the presence of massive coarse-grained deposits.

Figure 3: Graphic-core logs of the four cores collected in the Colombia trench. The dotted line is a correlation based on ^{210}Pb excess.

Figure 4: Graphic-core log of the first (top) 150 cm of core KAMA21. The X-ray image and its interpretative drawing reveal the presence of four main coarse-grained layers (B1 to B4) interpreted as earthquake-triggered deposits (see text for explanation). The age model is based on ^{210}Pb excess. The figure presents a) depth $^{210}Pb_{xs}$ profiles against depth in sediment, b) corrected $^{210}Pb_{xs}$ profiles against event-free depth (the thickness of each gravity-flow deposit was substracted from the total depth) and c) the CIC and CF-CS age model; error bars correspond to 1 SD, the lines in c correspond to min, mean and max CF-CS ages of hemipelagic sediments. The four main earthquakes that affected the north Ecuador/south Colombia margin during the 20th Century are located on the age model.

Figure 5: Photograph, X-ray image, grain-size (D50) and magnetic-susceptibility analyses illustrating the main features of Bed-Type 1 in core KAMA21. (A), (B), (C) are close-up views of the bed illustrating below. (A) is an X-ray image. (B) and (C) are thin-section images with increasing magnification.

Figure 6: Photograph, X-ray image, grain-size (D50) and magnetic-susceptibility analyses illustrating the main features of several superimposed beds of Type 1 in core KAMA21.

Figure 7: X-ray image, grain-size (D50) and magnetic-susceptibility analyses illustrating the main features of Bed-Type 2a in core KAMA21. This bed corresponds to B4 shown in Figure 3. Note the amalgamated character revealed by both grain size and magnetic susceptibility. (A), (B), (C) are close-up views of the bed illustrating below. (A) is an X-ray image. (B) and (C) are thin-section images with increasing magnification. They reveal the presence of an erosive surface (E.S.) separating the two superimposed intervals, and of cross-stratifications (C.S.) consisting of alternating coarser- and finer-grained laminae.

Figure 8: Photograph, X-ray image, and grain-size (D50) analyses illustrating the main features of Bed-Type 2a in core KAMA21. Note the amalgamated character revealed by the grain size and the alternation between laminated and cross-laminated intervals. (A), (B), (C) are close-up views of the bed illustrating below. (A) is an X-ray image. (B) and (C) are thin-section images with increasing magnification. They reveal the presence of erosive surfaces (E.S.) separating the superimposed intervals, and of cross-stratifications (C.S.) consisting of alternating coarser- and finer-grained laminae.

Figure 9: A) Photograph, X-ray image, grain-size (D50) and magnetic-susceptibility analyses illustrating the main features of two superimposed beds of Type 2a in core KAMA21. B) X-ray image, explanatory drawing and grain-size (D50) analyses illustrating the main features of Bed-Type 2b in core KAMA21.

Figure 10: A) Photograph, X-ray image and explanatory drawing, and B) X-ray image and explanatory drawing illustrating the main features of Bed-Type 3 in core KAMA21.

Figure 11: X-ray image, grain-size (D50) and magnetic-susceptibility analyses illustrating the main features of Bed-Type 4 in core KAMA05. Note the presence of rounded mud clasts scattered in the basal half of the bed.

Table 1: AMS radiocarbon data and sample age calibrations obtained in cores KAMA21, KAMA10 and KAMA05.

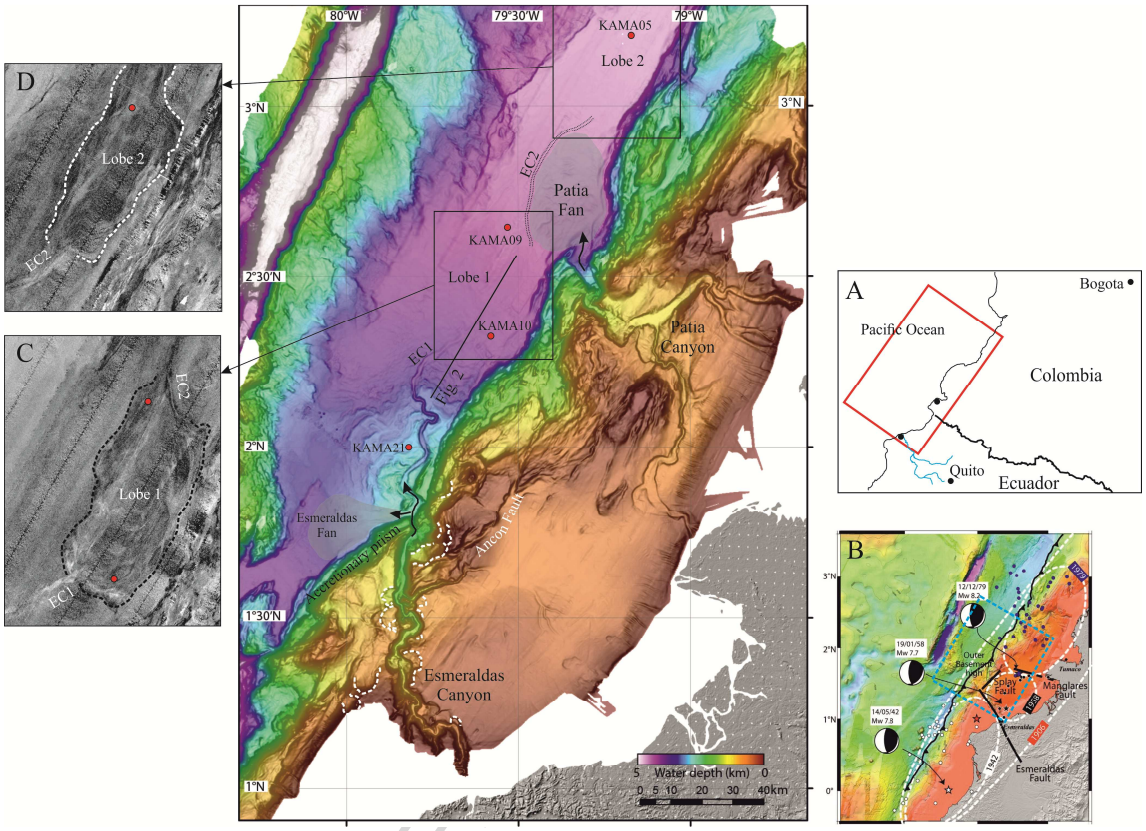

Fig. 1

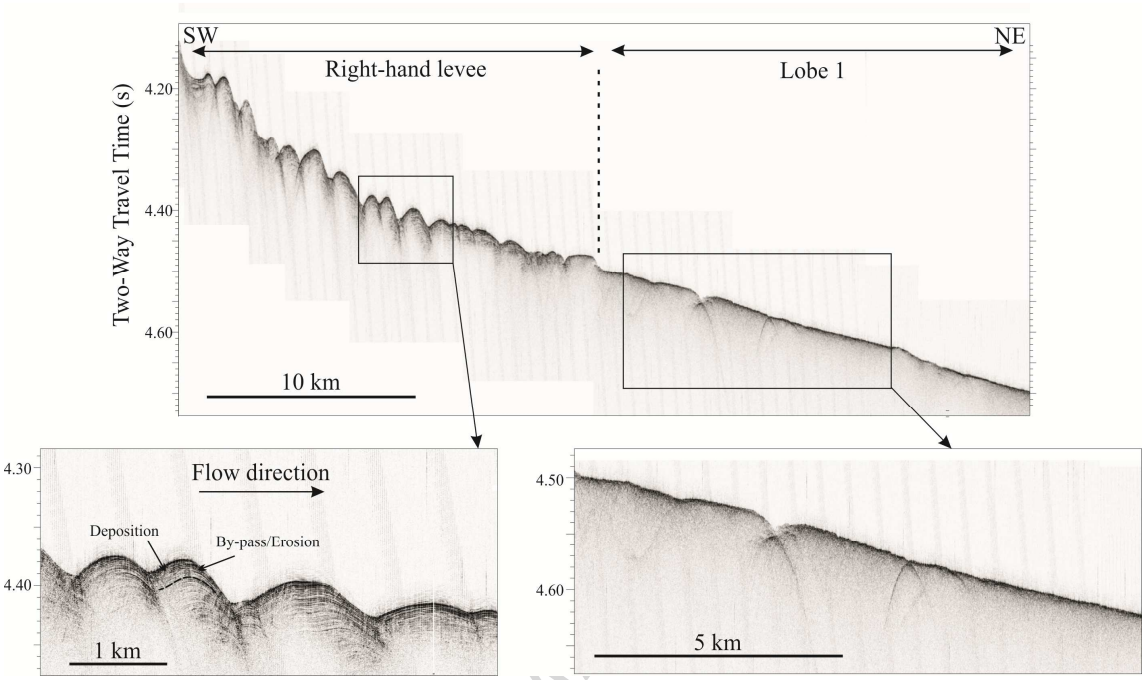

Fig. 2

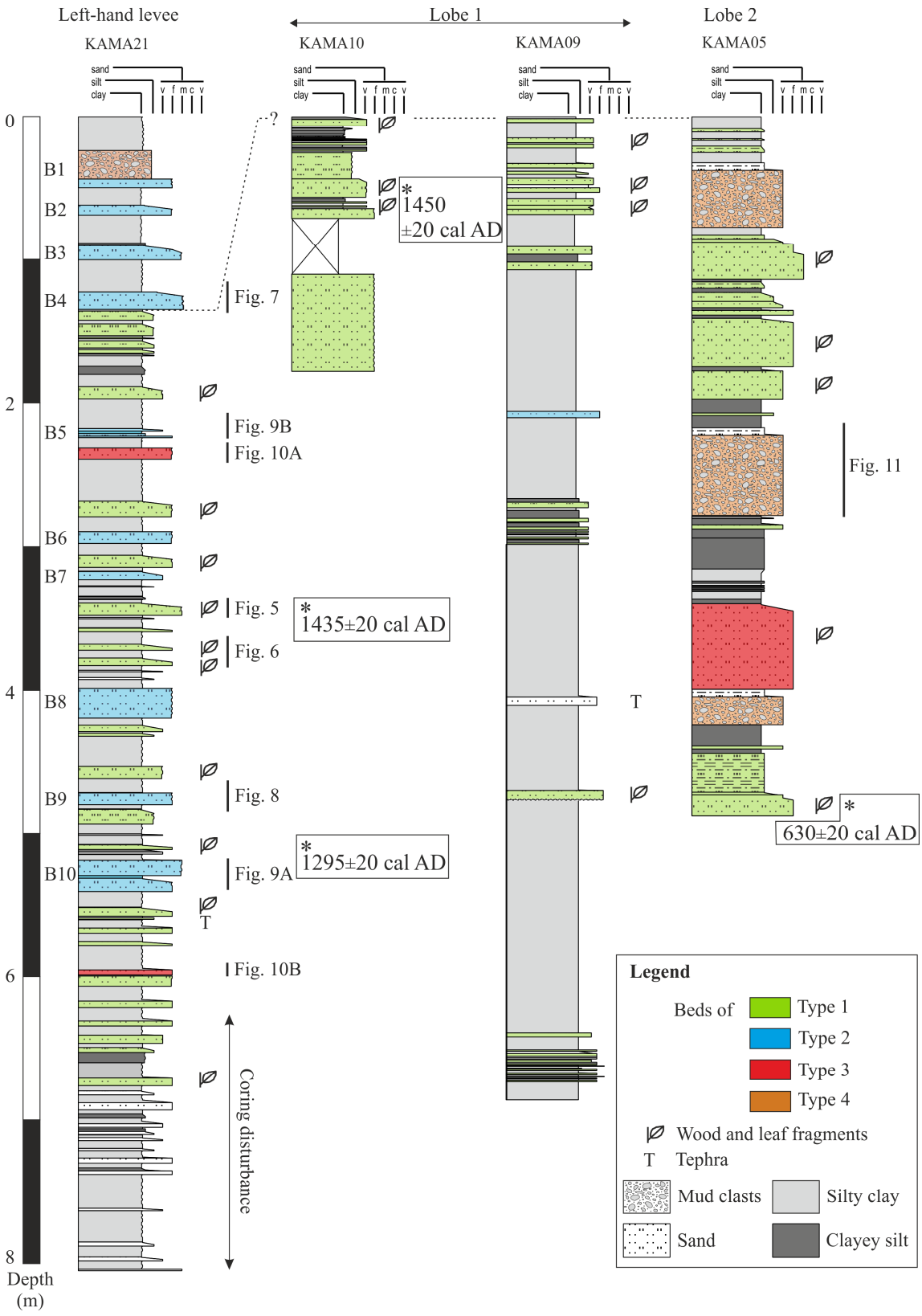

Fig. 3

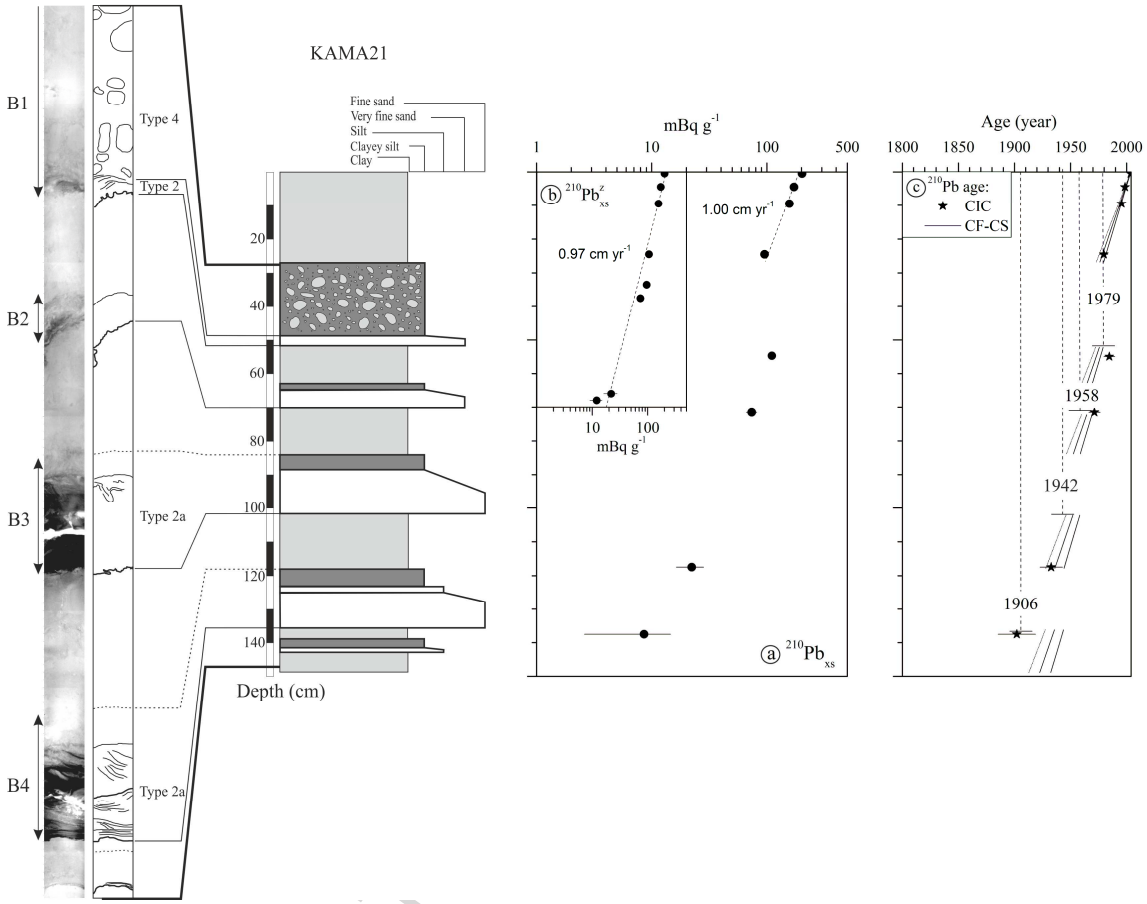

Fig. 4

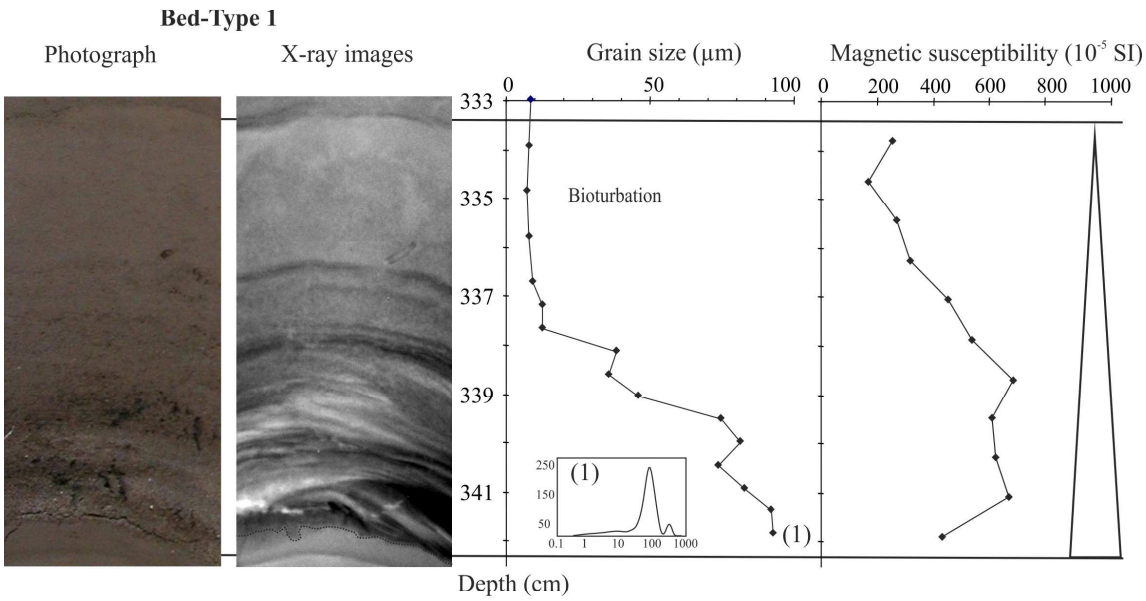

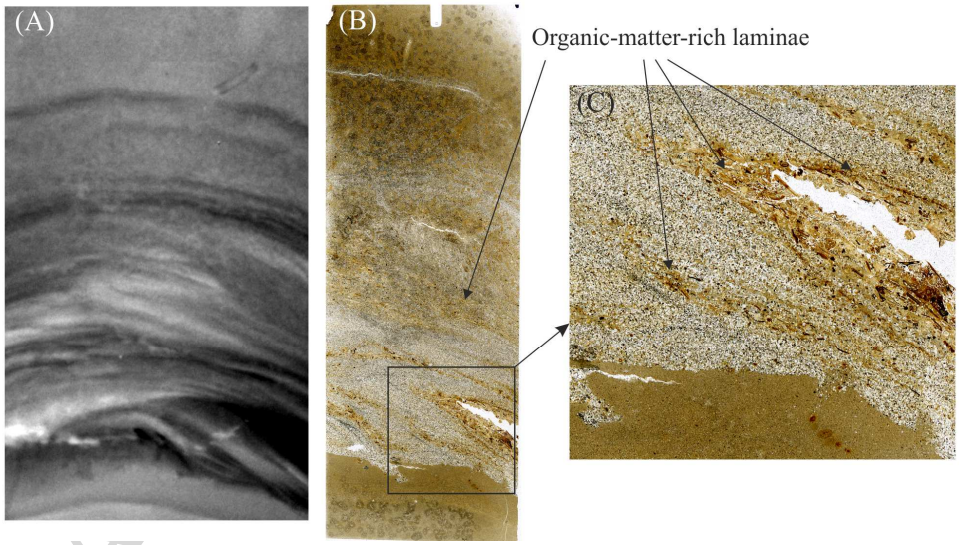

Fig. 5

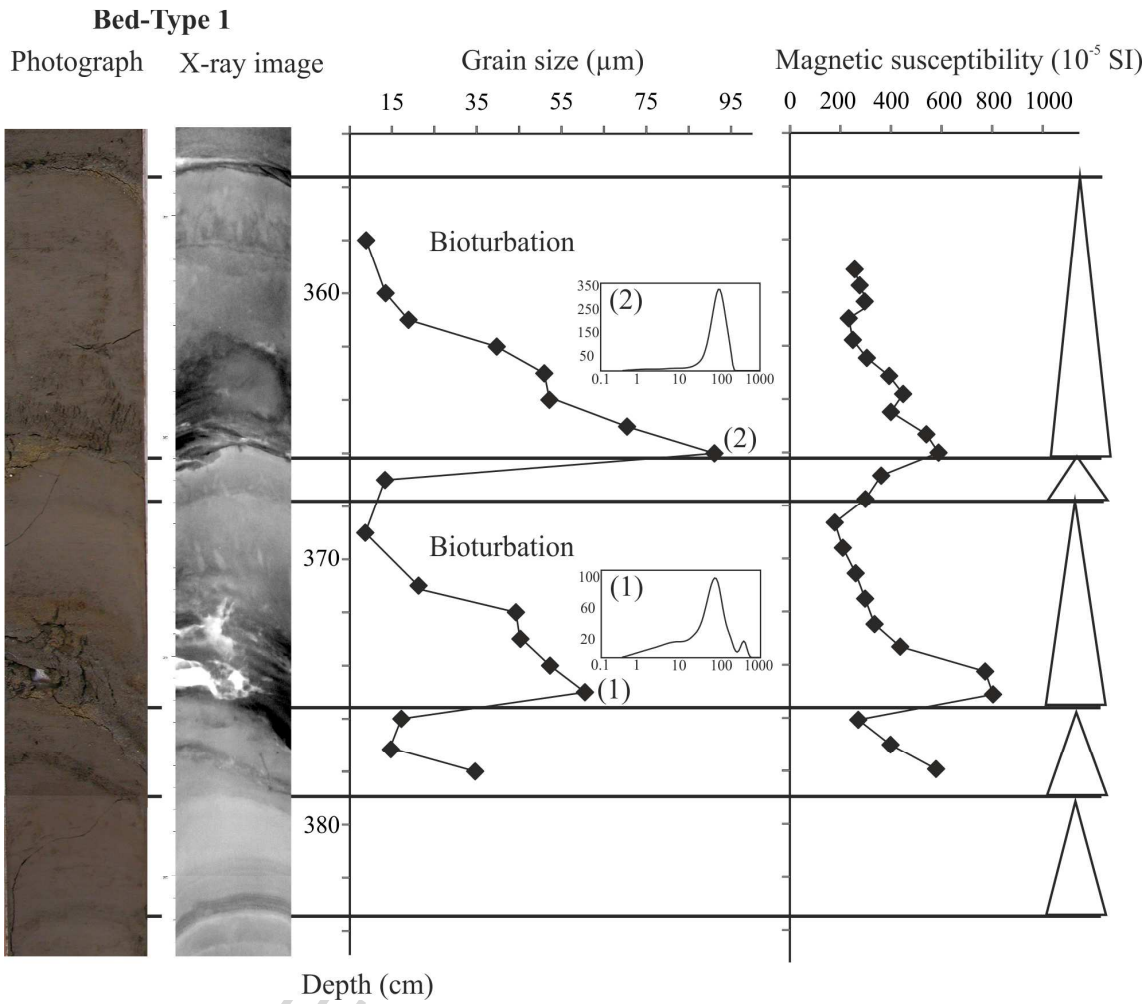

Fig. 6

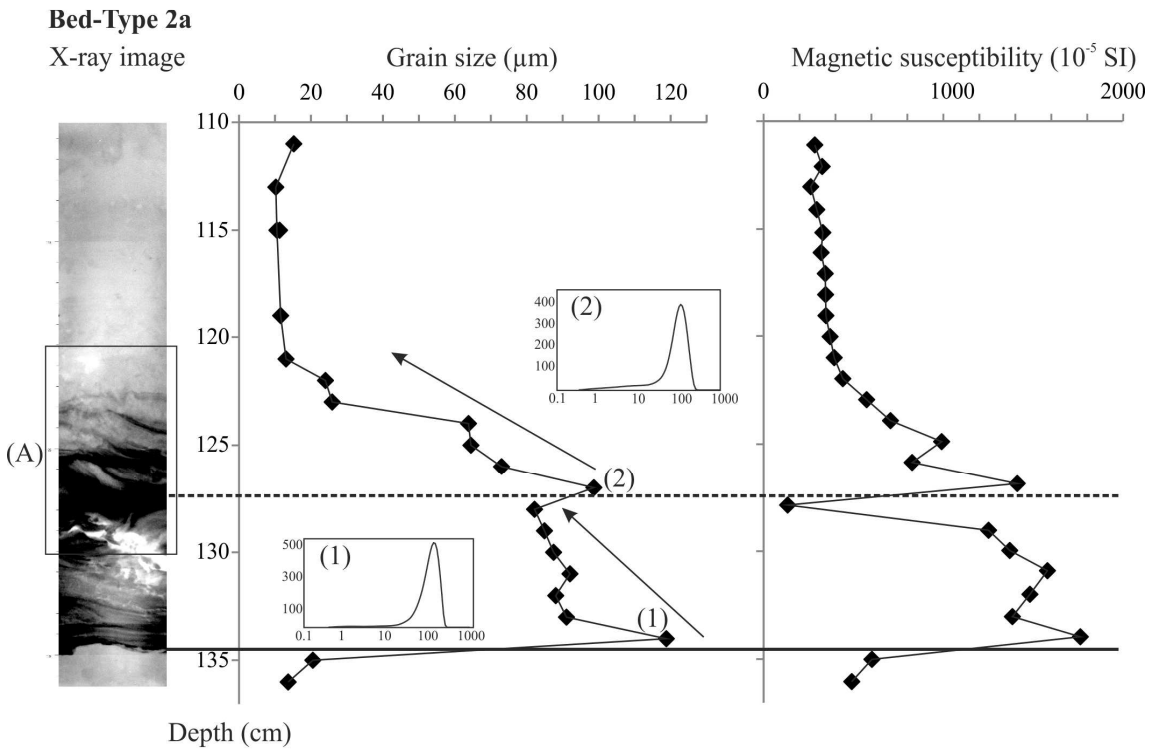

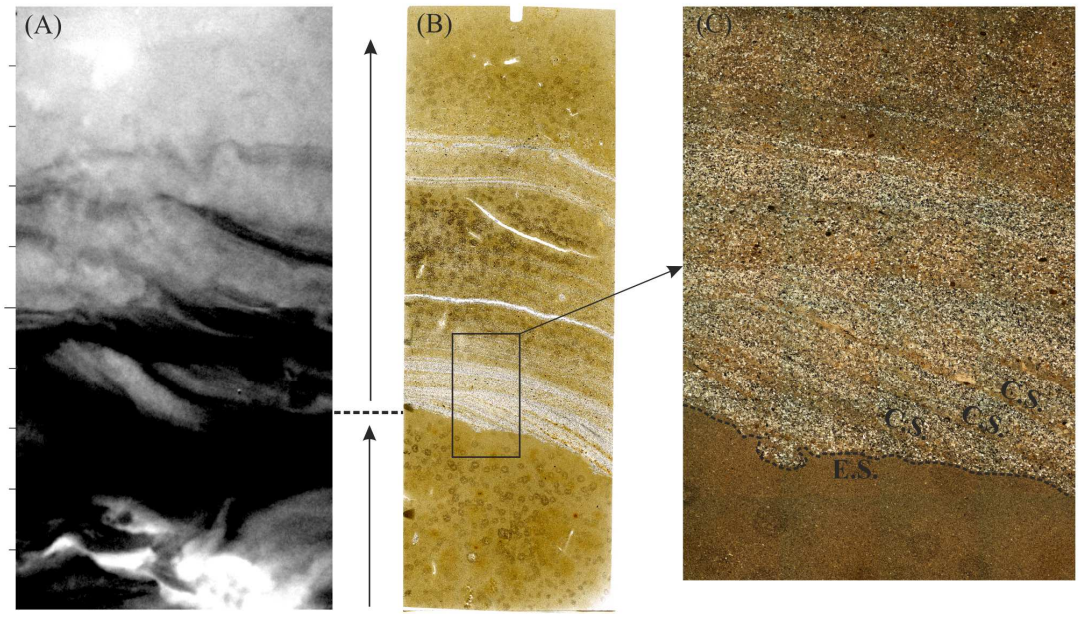

Fig. 7

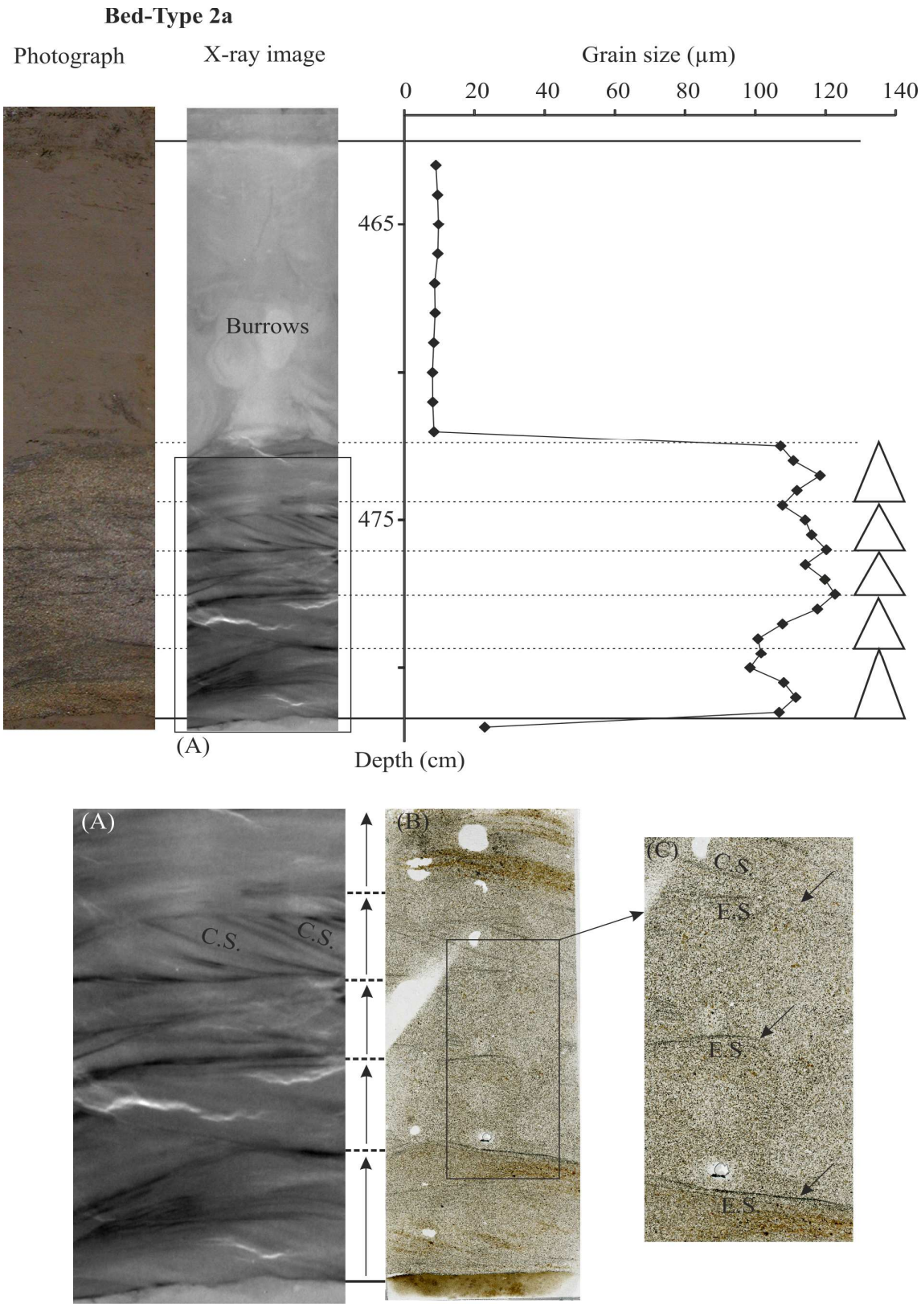

Fig. 8

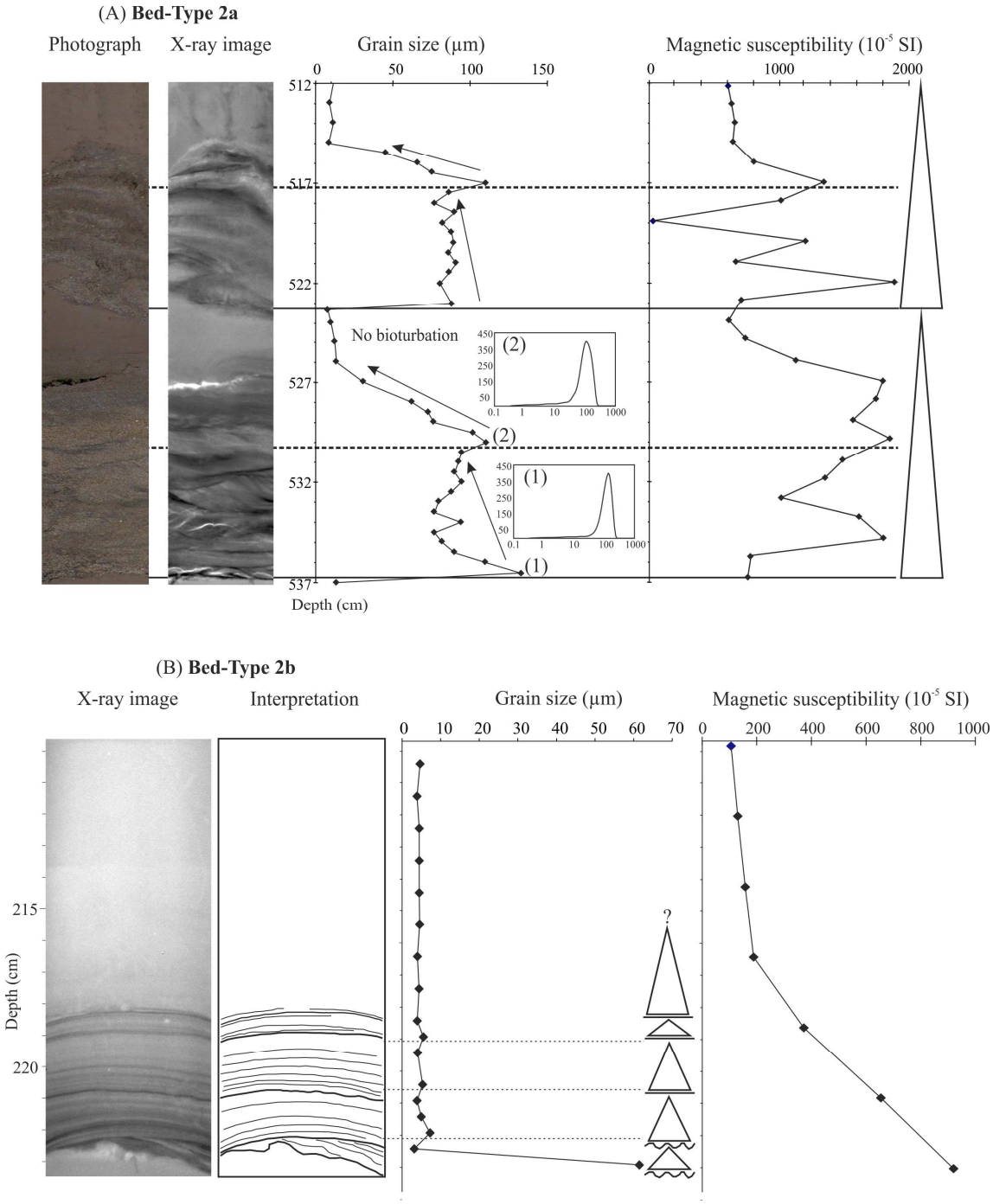

Fig. 9

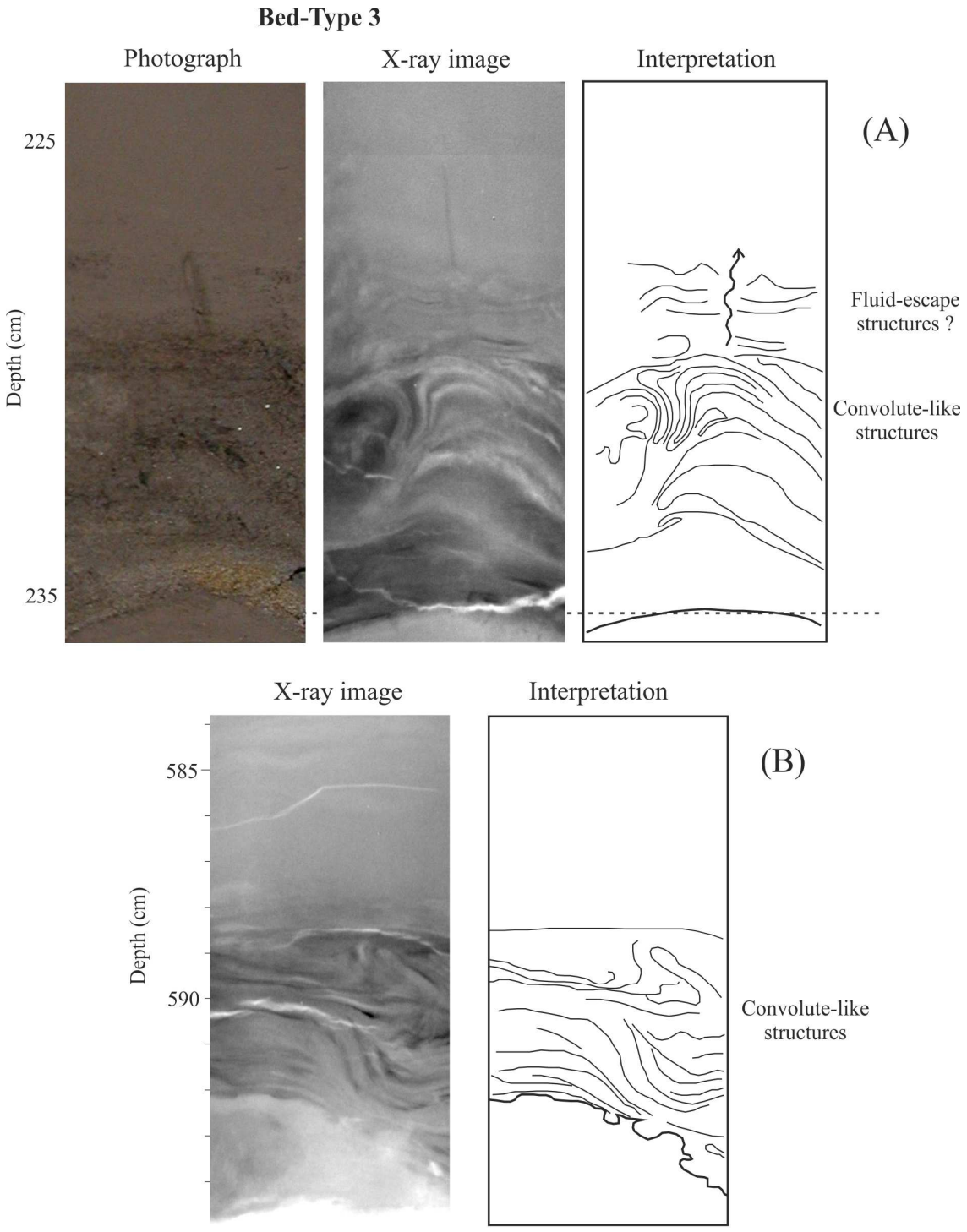

Fig. 10

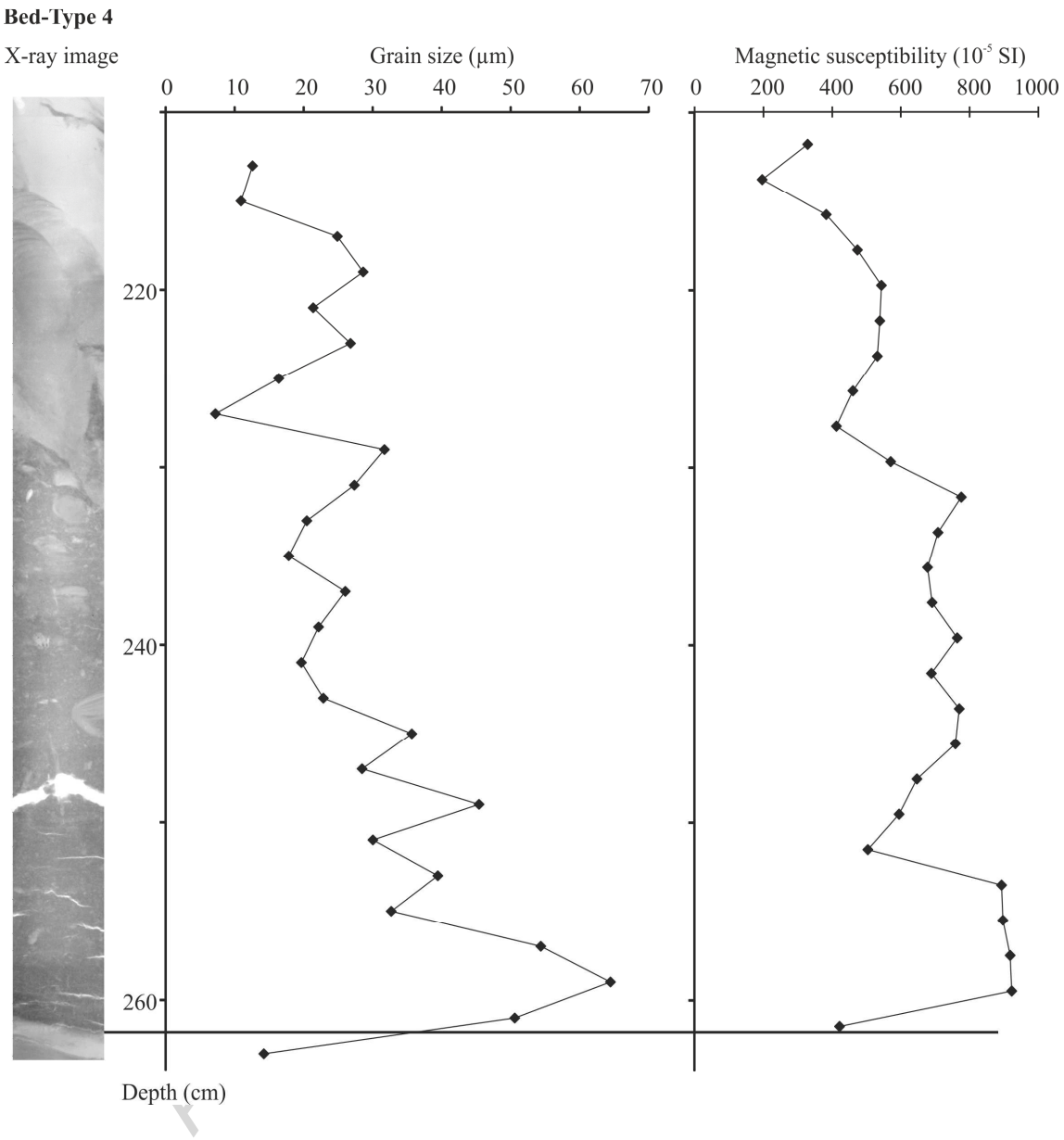

Fig. 11

Table 1

Cores	Water depth (m)	Core depth (cm)	Material	Radiocarbon age (year BP ± 1σ)	1σ Cal AD age
KAMA21	2954	342	Wood	460 ±30	1435
KAMA21	2954	521	Wood	670 ±30	1295
KAMA10	3395	31	Wood	425 ±15	1450
KAMA05	3811	465	Wood	1420 ±30	630